Impacts of afternoon and evening sea-breeze fronts on local turbulence, and CO_2 and radon-222 transport

Jon A. Arrillaga [a]*, Jordi Vilà-Guerau de Arellano [b], Fred Bosveld [c], Henk Klein Baltink [c], Carlos Yagüe [a], Mariano Sastre [a] *and* Carlos Román-Cascón [d]

[a] *Dept. Física de la Tierra, Astronomia y Astrofísica, Universidad Complutense de Madrid, Madrid, Spain*

[b] *Meteorology and Air Quality Group, Wageningen University, Wageningen, Netherlands*
[c] *Royal Netherlands Meteorological Institute (KNMI), De Bilt, Netherlands*

[d] *Univ. Grenoble Alpes, CNRS, IRD, Grenoble INP, IGE, F-38000 Grenoble, France*

*Correspondence to: Dept. de Física de la Tierra, Astronomía y Astrofísica, Facultad de Ciencias Físicas, Universidad Complutense de Madrid. Ciudad Universitaria, Plaza Ciencias 1, 28040 Madrid, Spain. E-mail: jonanarr@ucm.es.

We investigated sharp disruptions of local turbulence and scalar transport due to the arrival of sea-breeze fronts (SBF). To this end, we employed a comprehensive 10-yr observational database from the Cabauw Experimental Site for Atmospheric Research (CESAR, The Netherlands). Sea-breeze (SB) days were selected using a five-filter algorithm, that accounts for large-scale conditions and a clear mesoscale-frontal signal associated with the land-sea contrast. Among those days (102 in all, 8.3%), based on the value of the sensible-heat flux at the onset of SB, we identified three atmospheric boundary layer (ABL) regimes: convective, transition and stable. In the convective regime the thermally-driven convective boundary layer is only slightly altered by a small enhancement of the shear when the SBF arrives. Regarding the transition regime, we found that the ABL afternoon transition is accelerated. This was quantified by estimating the contributions of shear and buoyancy to the turbulent kinetic energy. Other relevant disruptions are the sharp reduction in ABL depth ($\sim$250 m h^{-1}) and the sudden increase in average wind speed ($>$ 2 m s^{-1}). In the stable regime the arrival of the SB leads to disturbances in the wind profile at the surface layer. We observed a deviation of more than 1 m s^{-1} in the observed surface-layer wind profile compared to the profile calculated using the Monin-Obukhov Similarity Theory (MOST). Our findings furthermore reveal the determinant role of the SB direction in the transport of water vapour, CO_2 and ^{222}Rn. The return of continental air masses driven by the SB circulation generates sharp CO_2 increases (up to 14 ppm in half an hour) in a few SB events. We suggest that the variability in ^{222}Rn evolution may also be influenced by other non-local processes such as the large-scale footprint from more remote sources.

Key Words: mesoscale; coastal meteorology; boundary-layer dynamics; afternoon-evening turbulent transition; scalar transport

1. Introduction

When large-scale forcings are weak and insolation is very important, the daytime cycle of the atmospheric boundary layer (ABL) is governed by local surface turbulence and entrainment from the residual layer (during the morning transition) and the free troposphere (Stull 1988). Under these conditions, the sea-land temperature contrast is increased in coastal areas, generating a sea-breeze (SB) circulation. The lower part of that circulation is manifested in the form of a density current, that usually propagates far inland around 50-60 km (Miller *et al.* 2003). Occasionally, it reaches further inland: as far as 100 km in The Netherlands (Tijm *et al.* 1999), or for instance, Soler *et al.* (2014) observed the arrival of density currents at the CIBA site (Spain) which is located 200-km away from the sea. SBs have been detected even further inland, for example by Hu and Xue (2016), who found that the sea-breeze front (SBF) reached Dallas (Texas, USA) at midnight, i.e. as far as 400 km inland. The arrival of the SBF led to a collapse of the urban-heat island and the breakdown of the nighttime surface inversion in rural areas. So depending on the local turbulence conditions, the impact of SBFs can be rather distinct.

The acceleration of the inland propagation of SBFs after the decay of the convective boundary layer (CBL) is a relevant aspect that is not as yet well represented by mesoscale models (Crosman and Horel 2010). Convective mixing within the CBL leads to frontolysis, and consequently to the slowing down of the propagation of SBFs (Grisogono *et al.* 1998). When daytime convection is weakened, however, the SBFs are reinforced again, and subsequently, the SBFs in the late afternoon and evening accelerate (Atkins and Wakimoto 1997). Although most SB studies focus on areas close to the coastline as far as 25 km inland (Atkins and Wakimoto 1997; Borne *et al.* 1998; Talbot *et al.* 2007; De Tomasi *et al.* 2011; Calmet and Mestayer 2016), in many locations further inland the arrival of the SBF takes place during the afternoon and evening transition of the ABL. During that process, there is a transition from daytime convective to nighttime stable conditions, and turbulence decays in a complex way, particularly in areas of complex terrain Lothon *et al.* (2014); Sastre *et al.* (2015). Only a few investigations of the ABL transition under SB conditions have been performed. Jimz *et al.* (2016) characterise the morning transition between the land breeze and the SB using both modeling and observations. They found that the transition occurs in four steps, but the model is incapable of capturing the observed evolution of the thermal profile. Cuxart *et al.* (2014) discovered that the SB below 200 m above ground level (agl) is the result of an equilibrium between the pressure gradient and turbulence. They analysed the terms of the turbulent kinetic energy (TKE) budget during the different stages of a SB case through numerical simulations. Arrillaga *et al.* (2016) found that a SB event that takes place after the convective decay, i.e. a late-sea-breeze event, showed different patterns than a SB occurring during convective conditions.

However, little attention has been paid to analysing the challenging interplay of the SB with local turbulence and scalar transport when the frontal passage occurs in the late afternoon and evening. Our investigation therefore aimed to shed light on the role of the SB during that critical stage within the diurnal cycle of the ABL, studying not just a single, but numerous SB events. For this purpose, we used the comprehensive observational database of Cabauw in The Netherlands (Van Ulden and Wieringa 1996). Since it is located sufficiently far away from the coast (∼ 50 km) and in a topographically flat area, it is an ideal site. To illustrate some of the challenges of our study, Figure 1 shows the evolution in time of the vertical distribution of aerosol backscatter in Cabauw obtained from a LD40 ceilometer, on a day characterised by well-mixed conditions and the development of a prototypical CBL. Around two hours before sunset, the convective regime was suddenly interrupted by the arrival of a well-formed SBF. In addition to the changes in the state variables, the SB flow advected a different aerosol layer. The mixing-layer height (MLH) estimates, shown by black dots, identify the collapse of the CBL. The wind-vector evolution from the wind profiler is represented in Figure 1b, which shows the veering of the wind from the SW to N-NW around 1700 UTC, confirming the SBF passage.

Inspired by this observational evidence, the main questions addressed by this analysis are:

- What is the impact of the SB on the boundary layer under the different ABL regimes? How do the afternoon and evening transitions respond to the SBF?
- How are the vertical and temporal distribution of scalars affected by the maritime-air-mass advection?

To answer these questions, we first performed an objective selection of SB events and grouped them together according to the time of arrival of the SBF and the surface turbulent regime at that time. This article is structured as follows: In Section 2 we describe the robust database employed. Section 3 explains the criteria employed to filter the SB occurrences, which aimed to select sufficient SB cases to obtain vigorous statistics. Section 4 discusses the main features of both local conditions in Cabauw and SB phenomena. Section 5 analyses the response of the ABL to the SB and quantifies the interaction with local turbulence for the different ABL regimes. In order to complete the dynamic description, the impact of the SB on scalar distribution is assessed in Section 6. We finish with the main conclusions and an appendix in order to further explain the data-treatment and observational analysis.

2. Observational site and data

Our study is based on a detailed analysis of 10 years of measurements (01/2001-12/2010) at the Cabauw Experimental Site for Atmospheric Research (CESAR), approximately in the center of The Netherlands (51°58'N, 4°56'E, -0.7 m above sea level (asl), see Figure 2). We focused on the warm period (May June July and August), since in these months the local forcings and mesoscale have a more noticeable influence in the ABL (Jimz *et al.* 2016). The North Sea is about 50 km W-NW of Cabauw, while the Markermeer, a shallow freshwater lake adjacent to the IJsselmeer lake, lies to the N-NE at approximately the same distance. Since the latter is very shallow (between 5 and 7 metres depth), its temperature is closely coupled to air temperature (Mooij *et al.* 2008): thus, the North Sea is the main potential driver of SB circulations on the Dutch coast. Figure 2 shows the spatial differences of the satellite-measured sea-surface temperature (SST) for a few consecutive SB days. It can be seen that the SST of the Markermeer and IJsselmeer are significantly higher than in the North Sea. However, the Markermeer and IJsselmeer lakes play an important role in the propagation of SBs as will be shown later. The area between Cabauw and the sea mainly consists of flat grassland (Tijm *et al.* 1999), although the densely populated metropolitan areas of Amsterdam-Utrecht and Rotterdam-The Hague are relatively close to the N-NE and W-SW respectively. In any case, the topography of the surrounding area is very flat, and therefore the mesoscale flows are unaffected by topography and the density currents that spread inland are driven purely by SBs, making this area an ideal site for the study of this phenomenon.

The observation site consists, first, of a 213-m tower located in a topographically flat agricultural area, free of surrounding obstacles (Beljaars and Bosveld 1997), although the roughness length varies with wind direction (Verkaik and Holtslag 2007). The soil is significantly wet throughout the year, with the water table lying about 1 m below the surface. The soil type in the southerly region of the tower is mainly river-clay, while north of the tower it is peat or peat on clay (Van Ulden and Wieringa 1996). Most of the ground is covered by grass or canals.

The Cabauw in-situ observational program that has been under way since 2000, allowed for the performance of several variables- and flux-measurements along the meteorological mast, covering the physical and dynamical aspects of the lowest part of the ABL. Apart from the 213-m mast, auxiliary masts and devices are available. Table 1 gathers all the variables measured in the present study, specifying the measurement devices employed, vertical levels and periods. For further information about technical aspects and other specifications of the CESAR site we refer the reader to Bosveld (2017).

One of the novelties of this work is the integration of the ABL depth from the estimation of the MLH. First, we analyse the MLH from a 10-year perspective, which is estimated from the aerosol backscatter measured by the LD40 ceilometer, mainly due to its continuing operational availability that provides robust and continuous databases. This device makes use of the LIDAR principle and is generally used to detect cloud bases. Moreover, the MLH can be estimated on the basis of strong vertical falls in the backscatter signal (e.g. Figure 1). The methodology employed to estimate the MLH is described in the Appendix.

For the SB cases, we employed MLH estimates derived from the radar backscatter profiles measured with the LAP-3000 wind profiler at Cabauw. This is a Doppler radar that is more reliable for detection of the MLH in the case of well-developed CBLs, which occur quite frequently on SB days. Unlike the estimates from the LD40 ceilometer for the 10-years period, the profile estimates were manually edited by inspection of the daily time-height radar backscatter data. The methodology employed to estimate the MLH based on the wind profiler is also detailed in the Appendix.

3. Selecting SB events from the 10-year database

The criteria employed to select the SB events were developed after the work of Arrillaga *et al.* (2016), in which SB events are characterised on the Cantabrian coast (north of Spain). Both the orographical and large-scale weather conditions are different from those in The Netherlands, and the criteria utilised have therefore been adapted to suit the local conditions. Table 2 presents the algorithm used to filter the SB events in Cabauw together with the total number of days that pass each of the filters, which are explained in detail here:

- Filter 1 eliminates the days with strong large-scale winds. Occasionally, when the large-scale wind is offshore (i.e. blowing from land to sea, in our particular case when the wind direction is between 45° and -225°), and above a certain threshold, the SB airflow does not reach land (Simpson 1994). When the wind is onshore, the SB component is masked by the large-scale wind and therefore very difficult to detect as an isolated phenomenon (Miller *et al.* 2003). For there reasons, several studies have defined an upper threshold for the synoptic wind speed above which the SBF passage is blocked. Numerical studies set that value within the range of 6-11 m s^{-1} (Crosman and Horel 2010). Since our aim was to remove all days with strong large-scale winds, we chose the lower value, i.e. 6 m s^{-1}. In order to derive the large-scale wind, we used data from ERA-Interim reanalysis at 850 hPa, because at that level the lower branch of the SB cell is unlikely to be detected (the typical maximum ABL depth in a SB day is around 1000 m). For instance, according to Atkinson (1981) the highest altitude at which the SB is detected is around 1.5 km. When computing the mean large-scale wind speed for each day, we only take into consideration the reanalysis values at 0600, 1200 and 1800 UTC, since the value at 0000 UTC does not affect the development of the SB circulation.

- Filter 2 discards the days that display a synoptical cold-front passage during the daytime. Cold fronts have features that resemble those observed in SBFs, for instance: a sudden veering of the wind and a sharp drop in temperatures. Indeed, synoptical fronts that pass when the intensity of the large-scale winds is below the defined threshold of Filter 1, could be filtered as SB. In addition, cold fronts are generally linked to rough weather, which of course is not the best scenario for the formation of SB. Synoptical fronts are hard to define objectively, and their depiction in weather pressure charts is actually rather subjective. However, Hewson (1998) defines synoptical fronts objectively using the horizontal gradient of the equivalent potential temperature and the wet-bulb potential temperature, amongst other ways. Taking both the latent heat of vaporisation and the specific heat at constant pressure for dry air ($l_v(15°C) = 2.46\times10^6$ J kg^{-1} and $C_{pd}(15°C) = 1005$ J kg^{-1}K^{-1} respectively) into account, we can assume the following for the tendency of the equivalent potential temperature θ_e:

$$\frac{\Delta\theta_e}{\Delta t} \simeq \frac{\Delta\theta}{\Delta t} + \frac{l_v}{C_{pd}}\frac{\Delta r}{\Delta t}, \qquad (1)$$

  where θ is the potential temperature and r the water-vapour mixing ratio, both obtained from reanalysis data at 850 hPa, for the abovementioned reasons. Taking into account the values of the horizontal gradients given by Hewson (1998) and a V_{850} of 5 m s^{-1}, which is regarded as adequate to describe the propagation speed of the cold fronts (bearing in mind that the cases in which $V_{850} > 6$ m s^{-1} are discarded), the days in which θ_e falls more than 1.45°C in 6 h (either from 0600 to 1200 or from 1200 to 1800 UTC) are regarded as being characterised by the passage of a synoptical cold front, and were therefore eliminated from the selection. We emphasise that the correctness of this filter was checked for a number of days in contrast with the fronts depicted in Met Office surface pressure charts, and produced convincing results.

- Filter 3 rejects the days in which precipitation greater than 0.1 mm is recorded between 0600 and 2200 UTC. Most of the days in which precipitation occurs have already been rejected by the previous filters, but some of them are characterised by fair-weather conditions, which may trigger convective-cloud development, and in some cases, storms. Such afternoon storms could produce gravity currents which may also be misinterpreted as SB, and we therefore needed to discard them. Even if these days included the passage of the SB, they would pollute the pure SB signal that we finally wish to analyse. Precipitation that occurs during the night does not affect the SB formation and passage; hence, we only consider precipitation measured between 0600 and 2200 UTC.

- Filter 4 assures that a certain sea-land temperature gradient is exceeded, as it is needed to trigger the circulation of SBs. Since we need the values of the air temperature over the sea, we employ 2-m ERA-Interim reanalysis data at 1200 UTC. At that time of the day, the land is sufficiently warm, and due to the distance from Cabauw to the sea (∼ 50 km), the SBF has not usually reached Cabauw. The value of 2°C was derived from the 10th percentile of all the SB days in the Cantabrian coast in Spain. Many other authors use higher thresholds to select SB days: 3°C in Borne *et al.* (1998) or 5°C in Wichink Kruit *et al.* (2004). However, they use the SST to compute the gradient, which was demonstrated to have a bias with respect to the air-temperature over the sea in Arrillaga *et al.* (2016). As a proxy for the air temperature offshore we use the ERA-Interim reanalysis value at a grid point over the North Sea (52.5°N, 4.25°E), approximately 20 km from the shore, and over land we choose the grid point closest to Cabauw (52°N, 5°E), both sites at 2 m asl.

- Finally, the last filter (Filter 5), requires a clear frontal signal in order to be finally selected as a SB day. In detail, there needs to be a change in the wind $\Delta\alpha$ to an onshore direction (i.e. blowing from sea to land) between 1000 and 2000 UTC, and one of the two conditions described in

Table 2 must be met. The wind has to be maintained in the onshore direction for at least two hours without oscillating too much around the wind direction after the shift. First, we define the onshore range taking into account the coastline orientation: [225°- 45°]. With respect to the time range, [1000-2000 UTC], we define it given the mean wind roses at different times (not shown here), and also taking into account that after sunset instead of a SB we would be having a late-SB. This filter is an adaptation of the last filter defined in the algorithm of Borne *et al.* (1998). The criteria are rather strict, since we demand a certain degree of confidence regarding the filtering of clear SBF passages.

4. Local scale and mesoscale in Cabauw

Before studying the complex interplay between the mesoscale phenomena and local turbulence, we first explore the average local conditions in Cabauw during the warm period, followed by the main characteristics of the selected SB events. Following the process of narrowing these down, we filter the clear SBF passages that occurred during this period and we explore their general aspects.

4.1. Ten-year analysis of the ABL

We started by evaluating the role of the local surface fluxes, i.e. sensible-heat (SH) and latent-heat (LH) fluxes, in the diurnal evolution of the potential temperature and specific humidity (from 1.5 to 200 m) for the warm period of the 10 years, as shown in Figure 3. The 10-year averages are calculated for each of the variables; in the case of the SH and LH fluxes, the averages are computed from series of observations that contain gaps, instead of using gap-filled data. Closely related to the fluxes and state variability, we show the ABL-depth estimation in De Bilt. In this study we utilised the ABL depth as the metric that integrates both local and mesoscale effects.

The vertical lines represented in Figure 3a indicate the limits of the three ABL regimes that are defined according to the value of the SH flux in the SB onset ("SB onset" and "SBF arrival" mean the same in this work). We distinguish between three different ABL regimes: convective, transition and stable. The first is defined when the surface SH at the onset fulfils the following conditions: $\mathrm{SH_{onset}} \geq 0.5\mathrm{SH_{max}}$, where $\mathrm{SH_{max}}$ is the diurnal maximum SH value; the stable regime when $\mathrm{SH_{onset}} \leq 0$ and the transition regime in the rest of the cases, i.e. when $0 \leq \mathrm{SH_{onset}} \leq 0.5\mathrm{SH_{max}}$. Employing this clasification, we explored how the impact of the arrival of the SBF varies depending on the local turbulence conditions. Prior to that analysis, we studied the mean local conditions in Cabauw within the warm period, i.e. before filtering for the SB days.

First, the surface energy balance in Cabauw is mainly radiation-limited due to the moisture surplus: the average Bowen ratio $\beta = \mathrm{SH/LH}$ reaches a value of $\simeq 0.35$ (Chapin *et al.* 2002), typical of irrigated grasslands, at the moment of maximum heating. The soil is very wet in the area of Cabauw and during the warm period a substantial evaporation ($\mathrm{LH_{max}} \sim 200$ W m^{-2}) takes place. The LH flux begins to increase before both SH and buoyancy fluxes are positive: thus, specific humidity (Figure 3c) starts to increase before potential temperature rises (Figure 3b). Moreover, the evaporated water is mixed within a shallow boundary layer until 2-3 hours after sunrise, which explains the morning peak observed in the specific humidity at around 0700 UTC at lower levels. Later on, when thermal turbulence is strong enough to produce convection and the growth of the ABL, drier air from higher levels is entrained. The maximum value of the surface heat fluxes is recorded at around 1200 UTC.

The evolution of the ABL depth is mainly driven by the buoyancy flux and the strength of the capping inversion. However, the MLH measurements from the ceilometer are also influenced by other factors, and the estimation of the ABL depth is therefore more challenging. For instance, during the morning and early afternoon, the signal-to-noise ratio level of the ceilometer is lower than at the end of the day, which explains the significant reduction in the rising trend between 1000 and 1300 UTC (just 50 m in 3h), in addition to the fact that the ceilometer fails to detect the top of the well-mixed convective layers. In fact, the mean daily maximum MLH lies at around 900 m. The measurement uncertainty for daytime clear-sky ABLs is around 75-100 m (de Haij *et al.* 2007). Furthermore, the mesoscale phenomena, in the form of SBFs in Cabauw, have a significant influence on the physics and dynamics of the lower atmosphere in the afternoon and evening, being in a two-way interaction with turbulence.

However, the large-scale forcing masks the arrival of the SBF in many cases, which does not occur on every day of the warm season. On the other hand, the arrival of the SB density current takes place at a different time depending on the day, and therefore the time-averages do not capture the real effect of the SB. We therefore needed to conduct an objective and systematic SB filtering by using the SB algorithm explained in Section 3. This enabled us to disentangle the clear mesoscale frontal passages independently, as well as their impact on the ABL. Once we identified the onset of the SB, we grouped the different events together, taking the arrival of the SBF as a reference.

4.2. Sea breeze phenomena

We first present the ability of the systematic algorithm to select the SB events (Table 2) by showing the percentage of the total number of days that pass each of the filters. Moreover, Figure 4 displays the wind roses at two times of day for each day that passed the individual filters of the algorithm: 1200 UTC and 1800 UTC. The first time is chosen for two reasons: it is roughly the time at which both surface fluxes have their maximum values and additionally, in most of the cases the SB onset has not taken place yet at Cabauw. With respect to the second time, it is close to sunset (the average SH flux is negative at this moment) and the SBF passage has already occurred in most of the cases.

The wind roses before the filters were applied are shown at the top of Figure 4. The 10-m wind measurement was employed. At 1200 UTC the predominant direction is SW, which is climatologically the most frequent and synoptically influenced (Sluijter *et al.* 2011). However, there is a clear predominance of all the westerly winds, which are affected by the sea-land temperature difference. It is likely that at this stage, the near-coastal diurnal acceleration (NCDA) defined in Jimz *et al.* (2016) accelerates the westerly component of the wind. A complete analysis of the contribution of the mesoscale phenomena in the wind diurnal variability was discussed in their study, but focusing on the NCDA. Jimz *et al.* (2016) analysed the rapid propagation of the inland wind-shift in the morning, which is directly related to the growth of the ABL onshore. However, we focus here on a distinct mesoscale phenomenon: sharp/clear SBF passages characterised by significant contrasts of temperature, humidity and wind speed, which are associated with the sea-land temperature gradient and take place in the afternoon/evening.

As shown in Figure 4b, two main wind directions emerge at 1800 UTC: NW and N-NE, which are linked to the two main SB directions. Filter 1 leads to many days being discarded ($\sim$ 69%), since The Netherlands is usually affected by large-scale perturbations throughout the year. Of the days that remain, most of them show a wind direction linked to either one of the two abovementioned SB directions at 1800 UTC (Figure 4d). At 1200

UTC, most of the SW-flow occurrences are excluded, and there is no any main direction at this time. After applying all the filters, we end up with 8.3% of the total amount of days being pure SB days, 102/1230 in total.

As stated, two main directions characterise the SB phenomena in Cabauw: NW and N-NE. Given the geographical location of Cabauw (see Figure 2), the former originates in the North Sea whereas the second seems to come from the closed Markermeer and IJsselmeer Seas. However, according to the satellite-derived SST, the latter seas are significantly warmer than the North Sea, and are therefore less prone to the formation of SB circulations. This suggests that the N-NE SBs are probably generated in the North Sea (north of the IJsselmeer) and subsequently propagated over these closed and shallow seas. On the other hand, the two SB directions are driven by different large-scale pressure patterns: for instance the N-NE SB develops under a high-pressure system over the north of the Netherlands, which induces a E-NE flow. The synoptic horizontal pressure gradient is therefore primarily responsible for the different SB directions.

Figure 5 shows the time of onset histogram of the SB for the filtered days, in coloured bars for the different months, and in black lines for the different wind directions just after the SB onset. Most of the SB passages take place between 1400 and 1900 UTC. This means that our data-set is adequate to study the role of the SB during the afternoon and evening transitions. Definitions of these transitions vary in the different studies (Lothon *et al.* 2014); in here, we define the afternoon transition as lying within the transition regime (SH > 0) and the evening transition within the stable regime (SH < 0). Moreover, the distribution of onset times differs from month to month. First, June is the month with the highest number of SB days (35% of the warm period), followed by July (26%), May (23%) and August (16%). June and July have longer periods of daylight, and they present a clear increase in the time of onset of the SB from 1500-1600 UTC on. In contrast, in August and particularly May, the increase is less clear and the differences between the time-range frequencies are smaller. On the other hand, the clear increase in the frequency of arrival of the SBF between 1400 and 1900 UTC could be a consequence of the acceleration of the inland propagation of SBFs that takes place in the late afternoon/early evening due to reduced convection, as has been suggested by some studies (e.g. Atkins and Wakimoto 1997; Crosman and Horel 2010). In any case, since we only analysed measurements at Cabauw that issue is not addressed in this study.

We separated the wind direction just after the onset into three different categories: NW, when it lays between 290° and -350°, N-NE between 350° and -45° and the latter value for remaining events (mainly W-SW). In 47% of the cases the wind blew from the N-NE, from the NW in 44% and 9% from other directions in the remainder. For the SB events in which the onset occurred with the wind from the N-NE or NW, we find a clear frequency increase for the aforementioned time range (1400 - 1900 UTC). The remaining events were almost equally spaced along the hours of daylight. There is a secondary peak in the N-NE SB distribution between 1800 and 1900 UTC which may be due to the Coriolis force, but at the same time the frequency of N-NE SBs was higher than the NW SBs between 1000 and 1300 UTC. Hence, although the influence of the Coriolis force in veering the wind clockwise has been reported in a few studies (Miller *et al.* 2003), we do not have enough evidence to support that statement and the role of Coriolis is still unclear.

The wind roses at 10 and 200 m agl at the onset of the SB are shown in Figure 6. The most intense SBFs at 10 m are those coming from the NW, which squares with the fact that the SST of the North Sea is colder than those of the inland seas (see Figure 2). However, at 200 m the wind rose shows strong SBFs from the NE (with a wind speed of up to 7-9 m s^{-1}), particularly between 22.5° and 45°. Furthermore, in a few cases the wind direction was offshore, i.e. between 45° and 225° at that height, indicating that while the SBF had reached the level of 10 m, it had not yet arrived at 200 m.

Despite the peak of SB events occurring during the afternoon/evening, the onset of mesoscale fronts takes place under distinct ABL regimes, as defined at the beginning of this section. The onset of SBs may occur either when the SH flux is around its maximum value (convective regime), when it is decreasing (transition regime) or even when it is already negative (stable regime). A chart showing the distribution of the SB events in the three regimes is shown in Figure 7. In Section 5 we analyse how the SBF impacts the ABL for the different regimes and we focus particularly on the challenging sinergy with local turbulence. Finally in Section 6 we explore another important aspect of the SB phenomenon: the impact of the different directions of the SBs on the advection of relevant state variables such as potential temperature and specific humidity, and scalars like CO_2 and ^{222}Rn.

5. Sea breeze-turbulence interaction in the ABL

Before dealing with the complex mesoscale-microscale interactions under each of the ABL regimes, we investigated the effect of the arrival of the SBF on the dynamic aspects of the ABL.

5.1. How does the ABL respond to the arrival of the SBF?

Figure 8 shows the impact of the SBF on the wind speed (a), potential temperature (b), specific humidity (c) and the ABL depth (d) for the three ABL regimes. For each of the regimes, we represented the mean of all the events normalised with respect to the onset of the SB. With t = 0 the first post-onset measurement, negative abscissa values indicate prefrontal time, while positive values identify postfrontal measurements. First, the wind speed confirms that the algorithm is capable of filtering out clear SBFs. It is interesting to observe that, during the short delay before the arrival of the SBF, a slight reduction in wind speed occurs due to the collision of the continental and maritime air masses, which is particularly evident in the convective regime. Under this regime, indeed, the trend of increasing wind speed is slightly altered by the SBF and the wind shear between the observational levels displays a slight increase. The change in the trend is evident in the potential temperature and even more so in the specific humidity. Before the SBF passage, q diminishes as convection entrains drier air from above the ABL; after the onset of SB, however, a moister air mass is advected and its value increases by over 0.5 g kg^{-1} in 10 min, especially at lower levels.

The behaviour of the lower atmosphere under the other two regimes is different. Under the transition regime, the wind speed after the SBF undergoes an abrupt increase particularly at higher levels, from less than 3 m s^{-1} up to more than 5 m s^{-1} within two hours. The most significant aspect, however, is the rapid increase in shear after the SBF: the difference between 10 and 200 m is less than 1 m s^{-1} before the onset and slightly over 2 m s^{-1} two hours later. We perform a more thorough quantification of the shear term in the following subsection. Moreover, the evolution of the potential temperature for this regime shows the transition from unstable to nocturnal stable conditions (from $\Delta\theta_{200\text{-}10} \simeq 0$ K before the SB onset to $\simeq$ 1K 2h after it), and the stratification of the specific humidity increases as well (from $\Delta q_{10\text{-}200} \simeq$ 0.45 g kg^{-1} before the onset to $\simeq$ 0.8 g kg^{-1} 2h after it). This suggests that the arrival of the SBF produces an acceleration of the ABL afternoon transition (SH > 0). Within the stable regime, however, the ABL evening transition (SH < 0) is also evident from the clear stratification of all the variables until the typical Nocturnal Boundary Layer (NBL) conditions are clearly met (see for instance Figures 8b-c two hours after the arrival of the SBF).

Nevertheless, the rise in wind speed particularly at higher levels (80, 140 and 200 m) prevents the formation of a highly stable NBL. In order to determine whether those features were actually due to the effect of the SB or were merely aspects of the evening transition under the stable regime, we compare SB and NSB days in Section 5.2.1.

With respect to the ABL depth (Figure 8d), which is regarded as the variable that integrates local and non-locally forced processes, we it this from the estimates of the MLH derived from LAP3000 wind profiler/RASS after a thorough manual editing. The passage of the SBF usually tends to result in a decrease in the MLH, while at the convective regime the MLH displays a sudden change in trend, evidenced by zero growth or even a slight fall after the SB onset. The effect of the SB is more evident under the transition regime, in which the MLH decreases substantially after the onset (~ 250 m/h), further reinforcing the hypothesis regarding the acceleration of the afternoon transition.

5.2. *Quantifying the interaction with local turbulence*

We now explore the complex interaction between mesoscale and local turbulence by employing scaling arguments appropriate for each ABL regime. We particularly stress the way in which the onset of the SB alters the transition to nocturnal stable conditions, depending on the degree of stability that the lower atmosphere has already reached.

We first present Figure 9, which shows the response of local surface turbulence to the passage of the SBF. The buoyancy flux, which is the measurement of the sonic-temperature flux, is displayed in (a), and the CO_2 surface flux in (b). We also include the friction velocity u_* (c), and the TKE and the variance of the vertical component of the wind σ_w^2 in (d). u_* is derived from the 10-m wind speed, the measured SH and the wind-direction dependent roughness length (Beljaars and Bosveld 1997; Verkaik and Holtslag 2007).

Both the buoyancy and the CO_2 fluxes are scarcely affected by the onset of SBs. Only in the stable regime does the trend appear to be slightly altered by the SBF, producing a sharper decrease in the buoyancy flux. On the other hand, u_*, TKE and σ_w^2 are affected by the passage of the front. For instance, u_* falls before the arrival of the SBF, particularly in the convective regime (Figure 9a). As we have already observed for the evolution of the wind speed (see Figure 8a), the collision of the maritime and continental air masses produces a moment of calm. After the passage of the front, u_* undergoes a sudden increase, especially under the stable and transition regimes: in the latter it increases by 40% within 2h, and in the stable regime, it increases almost by 50% in 1h, but decreases just afterwards. The TKE rises after the front, partially due to the increase in the vertical component σ_w^2 (Figure 9d). For example, the latter increases from 5 x 10^{-2} to 7 x 10^{-2} m^2 s^{-2} in the stable regime and from 12 x 10^{-2} to 16 x 10^{-2} m^2 s^{-2} in the convective regime just after the onset.

Assuming horizontal homogeneity and zero subsidence, the governing equation of the TKE ($=\overline{e}$) takes the following form (Stull 1988):

$$\frac{\partial \overline{e}}{\partial t} = \frac{g}{\theta_v}(\overline{w'\theta_v'}) - (\overline{u'w'})\frac{\partial u}{\partial z} - (\overline{v'w'})\frac{\partial v}{\partial z} - \frac{\partial}{\partial z}(\overline{w'e'}) - \frac{1}{\rho}\frac{\partial}{\partial z}(\overline{w'p'}) - \epsilon, \qquad (2)$$

where the term on the left-hand side denotes the trend, and the terms on the right are, from left to right, buoyancy, shear (two terms), TKE transport, pressure correlation and dissipation.

We have already explored how the surface turbulence is affected, but we lack validated flux measurements at the vertical levels of the tower for our 10-year period. However, based on the first-order closure we can infer the turbulent fluxes at the different levels by calculating the vertical gradients of measured variables:

$$\overline{w'\theta_v'} = -K_H \frac{\partial \theta_v}{\partial z}, \qquad (3)$$

$$\overline{u'w'} = -K_M \frac{\partial u}{\partial z} \qquad \overline{v'w'} = -K_M \frac{\partial v}{\partial z}, \qquad (4)$$

where θ_v is the observed 10-minute averaged virtual potential temperature and u and v the 10-minute mean horizontal wind components. The eddy diffusivities of heat and momentum K_H and K_M depend on the stability of the ABL. Since during the afternoon and evening transition of the ABL we are close to neutral conditions, we can assume that both coefficients are constant (Stull 1988). For our purpose and for the sake of simplicity, we consider both coefficients to be =1. As a result, we obtain alternative buoyancy and shear terms (hereafter referred to as B_* and S_*) along the tower levels:

$$B_* = \frac{g}{\theta_v}\frac{\partial \theta_v}{\partial z}, \qquad (5)$$

$$S_* = \left(\frac{\partial u}{\partial z}\right)^2 + \left(\frac{\partial v}{\partial z}\right)^2. \qquad (6)$$

To explore the impact of the SBF and to quantify the acceleration of the afternoon transition taking place in the transition regime, we calculate the temporal derivatives of both B_* and S_* as follows:

$$\frac{dB_*}{dt} = \frac{\partial \theta_v}{\partial z}\left(-\frac{g}{{\theta_v}^2}\frac{d\theta_v}{dt}\right) + \frac{g}{\theta_v}\frac{d}{dt}\left(\frac{\partial \theta_v}{\partial z}\right), \qquad (7)$$

$$\frac{dS_*}{dt} = \frac{d}{dt}\left\{\left(\frac{\partial u}{\partial z}\right)^2 + \left(\frac{\partial v}{\partial z}\right)^2\right\}. \qquad (8)$$

The temporal derivatives were computed using finite differences, while the vertical gradients of θ_v and the wind components u and v were derived from the method of least squares, which was applied to the generic scalar variable $\psi(z)$ in the following form (see Johansson *et al.* (2001); Steeneveld *et al.* (2005)):

$$\psi(z,t) = \alpha(t) + \beta(t)\ln(z) + \gamma(t)\ln^2(z) + \delta(t)\ln^3(z). \qquad (9)$$

The time-dependent coefficients were estimated at every observational measurement, i.e. every 10 minutes, and the vertical gradient $\frac{\partial \psi}{\partial z}(z,t)$ was computed at the intermediate levels: 15, 30, 60, 110 and 170 m agl. Since this method is sensitive to missing data (Steeneveld *et al.* 2005), we did not calculate the coefficients for the cases in which any of the vertical measurements were lacking.

In Figure 10, we represent dB_*/dt (a) and dS_*/dt (b) for the three ABL regimes at three intermediate levels: 30, 110 and 170 m. The 15-m and 60-m levels were excluded from the plot for the sake of simplicity: the first showed larger values than at other levels but its trend was equal to the 30-m level, whereas the second displayed behaviour intermediate between 30 m and 110 m. We also depict the trend of the temporal derivatives through regression lines, both before and after the onset of the SBs. Moreover, by exploring the second temporal derivatives of B_* and S_*, we infer whether the changes in both contributions occurred in an accelerated or decelerated manner. Note that in order to smooth the temporal series, 30-minute moving means were employed. Starting with the convective regime, the influence of the SB at higher levels is virtually non-existent. At the lowest level, i.e.

at 30 m agl, however, dB$_*$/dt increases just after the onset, and starts to decrease immediately afterwards. The increasing trend of S$_*$ is positive after the arrival of the SBF, but the dispersion of points implies that this trend is not particularly significant. A further analysis within the convective regime is discussed in Section 5.2.2.

In the case of the transition regime, the significance of the trends is stronger, particularly for B$_*$. The onset of the SB represents a minimum in the temporal evolution of dB$_*$/dt, as its trend is negative before and positive after the onset at the three vertical levels. This indicates that before the onset the lower atmosphere is decelerating towards a more stable state (d^{2}B$_*$/dt^2 < 0), whereas after the onset that acceleration becomes positive (d^{2}B*/dt^2 > 0), being slightly larger at the lowest level (d^{2}B$_*$/dt^2$\simeq$ +8.5$\times$10^{-6} s^{-3}/1h). On the other hand, dS$_*$/dt behaves differently at the lower and higher levels. Before the SB, S$_*$ at 30 m increases at a steady rate (dS$_*$/dt $\simeq$ 2$\times$10^{-5} s^{-3}), while it scarcely changes at 110 and 170 m. After the onset of the SB, however, S$_*$ at 30 m increases more rapidly (d^{2}S$_*$/dt^2$\simeq$ 1$\times$10^{-4} s^{-3}/1h). It also increases at the higher levels, but at a roughly constant rate (dS$_*$/dt$\simeq$ 1$\times$10^{-5} s^{-3}). Accordingly, we can unequivocally conclude that the arrival of the SBF in Cabauw accelerates the ABL afternoon transition when the convective regime is already decaying. In other words, the stabilisation of the lower atmosphere occurs more rapidly in the afternoon once the SB is established. Most of the SB studies have focused on early-afternoon SB cases and the interaction with convective turbulence (for instance Antonelli and Rotunno (2007); Comin *et al.* (2015)), but do not deal with the transition to stable nocturnal conditions. The role of katabatic flows as they interact with local turbulence during the afternoon-evening transition has certainly been observed and even modelled (e.g. Sun *et al.* (2006); Sastre *et al.* (2015); Lampert *et al.* (2016)), but such acceleration of the stabilisation process has not previously been documented. Moreover, the density currents arriving in Cabauw are unaffected by the topography, and we can be sure that this particular situation can only be attributed to the SB phenomenon.

With respect to the stable regime, the state that precedes the SB is different from that in the other regimes, and B$_*$ increases more rapidly at the three vertical levels (for instance d^{2}B$_*$/dt^2$\simeq$ +1.5$\times$10^{-5} s^{-3}/1h at 30 m), which is consistent with the fact that SH is negative or close to being so. Note that this pre-SB situation is what results after the arrival of the SBF in the transition regime. Comparing this situation with the transition regime; in the stable regime, the reaction of the lower atmosphere to the passage of the maritime gravity current is far from being identical: the SB produces a deceleration of dB$_*$/dt. At 110 and 170 m dB$_*$/dt decreases shortly after the onset, while at the lowest level the rising rate is merely reduced by around +0.5$\times$10^{-5} s^{-3}/1h. The shear term, S$_*$, continues to increase but more slowly, largely during the first 20-30 minutes after the onset. These results suggest that the evening transition could be somewhat slowed down, contrasting with the afternoon transition. Therefore, whether the SH flux is positive or negative is a key factor in determining the reaction of the lower atmosphere to the SB.

We have already shown that the SB produces an acceleration of the ABL afternoon transition, but the effect on the stable and convective regimes is still unclear. We therefore explore both regimes in detail below.

5.2.1. *Stable regime*

The clear increase in the wind speed and surface turbulence in the stable regime (see Figures 8 and 9), invites to conjecture that the equilibrium profile within the surface layer could somehow be disrupted by the arrival of the density current. We further explore this possibility in Figure 11, where we compare the evolution through time of the wind-speed difference between 80 and 10 m using both the similarity relations within the surface layer and the real observed differences, after the passage of the SBF. If both differences are similar, the wind profile is in equilibrium with local turbulence. If not, it means that an external factor brings it out of equilibrium: in this case the SB.

We assume the turbulent fluxes in the surface layer to be constant with height and dependent on gradients and the stability parameter $\zeta = z/L$ through universal dimensionless functions, where z is the height agl and L is the Obukhov length defined as:

$$L = \frac{-u_*^3\,\theta_v}{\kappa g\,\overline{w'\theta_v'}}, \tag{10}$$

where u_* is the friction velocity, θ_v is the virtual potential temperature measured at each height, κ is the Von Kármán constant (=0.4), g is the gravity acceleration (=9.81 m s^{-2}) and $\overline{w'\theta_v'}$ is the virtual-potential-temperature flux. Since we are considering that $\theta_v = T_v + 0.0098z$, we can assume that $\overline{w'\theta_v'} \simeq \overline{w'T_s'}$, where T$_s$ is the sonic temperature, which is almost equal to virtual temperature. According to the Monin-Obukhov similarity theory (MOST), the turbulent fluxes can be expressed in terms of the corresponding gradients, which are assumed to be proportional to the universal functions of ζ. For the specific case of the resultant wind speed U, we assume that:

$$\frac{\kappa z}{u_*}\frac{\partial U}{\partial z} = \Phi_M(\zeta). \tag{11}$$

The relationship between the gradient function (Φ_M) and the stability profile function Ψ_M is:

$$\Phi_M = 1 - \zeta\,\frac{\partial \Psi}{\partial \zeta}. \tag{12}$$

By integrating Eq. 11 between two vertical levels z_1 and z_2, we get the following equivalence:

$$U(z_2) - U(z_1) = \frac{u_*}{\kappa}\left\{ ln\left(\frac{z_2}{z_1}\right) - \Psi_M(\zeta_{z_2}) + \Psi_M(\zeta_{z_1})\right\}. \tag{13}$$

Under stable conditions ($\zeta > 0$), Holtslag and Bruin (1988) proposed an empirical form for Ψ_M given by:

$$\Psi_M(\zeta) = -b\left(\zeta - \frac{c}{d}\right)\exp(-d\zeta) - a\zeta - \frac{bc}{d}, \tag{14}$$

with $a = 1$, $b = 2/3$, $c = 5$ and $d = 0.35$.

On the other hand, in order to determine whether the disruption of the equilibrium in the profile is caused by the arrival of the SBF rather than by the decoupling of the different layers in the NBL, we compared the SB days in the stable regime with non-SB days (hereinafter NSB days). Before selecting the NSB cases, we first computed the time-lag between the sign change of the SH flux (t$_0$) and the SBF arrival (t$_{\text{SBF}}$) for the 22 SB days under the stable regime: $t_{\text{SBF}} - t_0$. Then, among the days that passed Filter 4 of the algorithm but were rejected by Filter 5 (see Table 2), we selected those ones when the wind was offshore (i.e. within the range 45°-225°) at least between t$_0$ for those days and the last t$_{\text{SBF}}$ of the SB days. To this end, we selected 31 NSB days that fell under the stable regime that we knew for certain that were not affected by the SB. Just as we normalised all the SB events with respect to the SB onset in order to compute the averages, we also normalised the NSB events with respect to an artificial SB onset. To do so, we created 22 new events for each NSB day, shifting their time dimension by the quantity $t_{\mathrm{SBF}} - t_0$ obtained from the 22 SB days. In this way, we normalised the NSB days with reference to an artificial SB onset so that SB and NSB days would be comparable under the modus operandi followed in this work.

Employing Eq. 13 we estimated the wind-speed difference between the observational levels of 80 and 10 m agl for both the SB and NSB days, and we represented them together with the REAL observed differences in Figure 11, after the appropriate normalised averages. For the NSB days the observed ΔU follows the MOST ΔU, and indicates that without the perturbation of a mesoscale flow the wind profile is controlled by the local turbulence. However, on SB days the wind profile departed from the MOST lead by the flow disturbances due to the arrival of the SBF, and is therefore no longer controlled by local turbulence. A representative example is the difference between the average MOST and REAL ΔU of up to 1 m s^{-1} 10 mins after the arrival of the SBF. The difference is thereafter reduced progressively, suggesting that the equilibrium is gradually being restored.

We further explored how local turbulence is modified by the SBF under the stable regime by calculating the mean shear capacity (SC) again for the SB and NSB cases, in this case at the five intermediate vertical levels. This dimensionless quantity was first introduced by van Hooijdonk *et al.* (2015) and it compares the measured shear with the minimum shear to maintain a continuously turbulent state, which is given by the energy demand at the surface. It is used to predict the regime transition from the continuously turbulent boundary layer (or weakly stable boundary layer) to the very stable boundary layer, or viceversa. Derived from the TKE budget equation (Eq. 2) by ignoring the transport terms, the SC is defined as:

$$SC = \left\{ \frac{(\kappa z)^2 \left(\frac{\partial U}{\partial z}(z)\right)^3}{g/\theta_0 \; |\overline{w'\theta_v'}|} \right\}^{1/3} , \tag{15}$$

where θ_0 is a reference potential temperature (we set a constant value of 293 K), κ is the von Kármán constant (=0.4), z is the height agl, $\frac{\partial U}{\partial z}(z)$ is the wind shear, g the gravitational acceleration (9.81 m s^{-2}), and $\overline{w'\theta_v'}$ is the downward surface kinematic heat flux, since SC is defined only when $\overline{w'\theta_v'} < 0$. The wind shear was computed using the method of least squares according to Eq. 9, but in this case for the wind speed itself, not the horizontal wind components as for dS$_*$/dt.

We represent the SC for both SB and NSB days between the time before the SB onset and 2h after in Figure 12. First, in the NSB cases (Figure 12b) SC increases particularly at the intermediate levels of 30 and 60 m, for instance in the latter case from 2.25 before the artificial SB onset to 4.25 2h after it. From observations at 20 m van Hooijdonk *et al.* (2015) found SC values that lay roughly between 2-3 and 3.5-5 for the very stable NBL and weakly stable NBL respectively. Hence, we can conclude that as an overall behaviour there is a tendency towards a continuously turbulent state in Cabauw on NSB days. This dimensionless number shows a distinct behaviour for the SB events. Interestingly, the SC displays a decrease at the very moment of the onset at the lowest (15 m) and highest levels (100 and 160 m), subsequently spreading to the 30 and 60 m levels. Moreover, there is a clear increase after the onset of about 1.5 at 160 m, followed by a fall of similar magnitude. These evolutions suggest that due to the disruption of the wind-profile equilibrium, the balance between the wind-shear profile and the surface SH flux is altered, until the momentum flux in the surface layer is able to restore the balance. In spite of the decrease of dS$_*$/dt (Figure 10b), the ability of mechanical turbulence to sustain the turbulent steady state is increased, and there is a general trend towards a more continuously turbulent NBL in the SB cases.

Hence, our analysis shows that the ABL regime in which the onset of the SB occurs is critical to determine its impact. Whether the SH flux is positive or negative when the SBF arrives during the afternoon-evening transition is actually fundamental, and involves contrasting consequences.

5.2.2. *Convective regime*

Finally, we explored how the characteristic convective scales of the well-mixed boundary layer were affected by the passage of maritime density currents. We explored two representative free-convection scaling factors (w_*/u_* and σ_w/w_*), and a time scale t_* in Table 3. w_* is defined as the free-convection scaling velocity (Deardorff 1972):

$$w_* = \left(\frac{g Z_i}{\theta_v} \, \overline{w'\theta_v'} \right)^{1/3} , \tag{16}$$

where in Z$_{\mathrm{i}}$ we substitute the MLH obtained from the wind profiler (see Figure 8d), θ_v is the virtual potential temperature at 2 m, and $\overline{w'\theta_v'}$, in contrast to Eq. 15, is the upward surface kinematic heat flux, for which the sonic-temperature flux is employed as previously justified. w_* is only defined when $\overline{w'\theta_v'} > 0$, but under the convective-regime that requirement is always fulfilled within the range between two hours before and two hours after the SB onset. This velocity has widely been used as a convective scale (Deardorff 1972; Moeng and Sullivan 1994; Calmet and Mestayer 2016): in Table 3 we present the calculated values of both the vertical-velocity standard deviation σ_w normalised by w_*, and w_* normalised by the friction velocity u_*. In addition, we calculated a representative time scale (t_*) for the eddies within the convective regime. Depending on whether the CBL is buoyancy- or shear-driven the time scale is calculated as $t_{*b} = Z_i/w_*$ or $t_{*s} = Z_i/u_*$ respectively.

Table 3 shows the range of values for the abovementioned scaling both during the 2-h period before and after the arrival of the SBF. The slight increase in the shear (see Figure 10b) after the arrival of the SBF induces a slight decrease in w_*/u_* ranging from 0.6 to 0.8 (Table 3). This scaling factor is a measure of the buoyancy-driven turbulence relative to shear-driven turbulence. When the stability parameter $-Z_i/L$ is very large, indicating the presence of a free-convection like state, then $w_* >> u_*$ (Wyngaard 2010). Other studies, for instance Deardorff (1972) found that $w_*/u_* > 2.2$ for a CBL in a buoyancy-driven regime, whereas Moeng and Sullivan (1994) set that value at 1.6 for a regime in which both shear and buoyancy dominate. Therefore, we can assume that the SB does not bring the buoyancy-driven CBL down, although it shifts it closer to the shear- and buoyancy-driven regime. Moreover, the upper range of σ_w/w_* increases to up to 1.3 after the SB as a consequence of the increase in σ_w. Most studies have found a value around 0.6 (e.g. 0.67 in Lenschow *et al.* (1980)) for a buoyancy-driven regime, which is within the range of values we observed. With respect to the representative time scale, we calculated it assuming a buoyancy-driven CBL ($t_* = Z_i/w_*$), and it represents the time needed for a thermal to rise. We obtained a range of values between between 15 and 30 min before the SB onset. After the onset, these values oscillate between 15 and 35 min, so we can conclude that the time scale of the eddies within the CBL is generally constant. Those values are close to those given for instance by Lenschow *et al.* (1980) (17 min) or Deardorff (1972) (15 min), which are representative of the turbulent scales within the CBL.

6. Impact on scalar transport

Finally, we studied another relevant aspect of the dynamic analysis: the influence of the direction of the SB on the transport of scalars and state variables ($\psi(t)$). Figure 13 shows box plots of the change in their values during the onset, given by $\Delta\psi = \psi(t_{\text{onset}}) - \psi(t_{\text{onset}} - 1)$, with respect to the wind direction $\alpha(t_{\text{onset}})$, gathered into six different subranges within the onshore range of 225° - 45°.

First, we show the change in air temperature (Figure 13a) and specific humidity (Figure 13b) during the onset. To be consistent with the wind-direction measurements which were taken at 10 m, the lowest height, we employed the 10-m measurements of both the specific humidity and temperature. In some SB events, particularly from the N-NW, the temperature fall is significant, between 1°C and 2°C in only 10 minutes, although it slightly increases in a few of them. In fact, Figure 8 shows how under diurnal convective conditions the cooling effect of the SB can be very slight or even absent. Specific humidity increases in most cases, being particularly significant for some N-NE SBFs (up to 3-3.5 g kg^{-1}). Besides, for those directions we also find the largest variance, and in fact, few specific-humidity decreases are observed. To explain the significant increases, on the one hand the SST of the IJsselmeer and Markermeer is considerably higher than in the North Sea (Figure 2), and the air over warmer seas has a greater specific humidity due to its higher evaporative capacity. Consequently, the SBs that pass over these enclosed seas bring a more humid air mass with them. On the other hand, N-NE SBs are generally driven by E-NE large-scale flows. Since air masses with an easterly origin are drier, the specific-humidity jump that accompanies the onset of SBs is larger.

We also explored the role of the SB in modifying the evolution of scalars such as CO_2 and ^{222}Rn in Figures 13 (c,d) and 13 (e,f) respectively. We analysed their concentrations at both 20 m and 200 m agl, since they are affected by distinct flux footprints and the amplitude of their diurnal cycle is also different. The measurements for these atmospheric compounds were performed every 30 minutes, while the wind direction was recorded every 10 minutes. The onset is defined taking into account the wind veering in Filter 5 of the SB algorithm, which is obtained from the 10-minute wind direction. We therefore always defined the SB onset for these scalars considering the next 30-minute value, in order to be sure that the SB had already arrived.

No significant changes in CO_2 concentrations changes were observed at the onset of SBs, except for a couple of SBFs from the W-NW [285° - 315°], in which a substantial jump (around 8 and 14 ppm) was measured at 20 m. In both cases the large-scale flow on the previous night had a continental origin and the SB arrived during the stable ABL regime. At 200 m, the greatest rises and falls of around 4-6 ppm are observed for both W-NW (285° - 315°) and N-NE (15° - 45°) ranges, coinciding with the directions of the main water bodies (see Figure 2). Previous studies in The Netherlands found higher CO_2 concentrations during E-SE continental flows, for instance Super *et al.* (2017) and Casso-Torralba *et al.* (2008) derived from measurements at Cabauw. Regarding other locations, for example Pérez-Landa *et al.* (2007) measured lower CO_2 concentrations during the SB stage in Valencia (on the Mediterranean coast of Spain), since the shallow marine air mass is affected by the uptake by plants. However, as pointed out by Ahmadov *et al.* (2007), the measurements of pollutants at coastal sites are not always representative of a large-scale footprint, but are so for the characteristic recirculation of the SB. This statement is indeed backed by a few studies: Gangoiti *et al.* (2001) linked the recirculation of tropospheric O_3 to land/sea-breeze circulation patterns, and Millet al. (1991) found that the tracers released in the morning returned with the SB of two days later.

Returning to Cabauw, of the cities with more than 250.000 inhabitants in The Netherlands, the city of Amsterdam is located to its N-NW, Rotterdam the SW, The Hague to the W and Utrecht to the NE (see Figure 2). According to the findings discussed above, the most plausible explanation for the observed jumps in CO_2 is the return of continental air masses rich in CO_2 through the SB circulation. Since the higher CO_2 concentrations are associated with offshore flows, they transport the CO_2 over the North Sea during the night. On the following day, if a SB circulation is formed and the SBF arrives in Cabauw, it may induce a sudden increase in the concentration of CO_2, particularly when surface conditions are stable, since the CO_2 is concentrated in the lower layers.

Regarding the ^{222}Rn, shown in Figure 13 (e, f), we calculated the changes from 30 minutes before the onset until 1 h after, i.e. in 90 minutes. We chose a longer time step than for the CO_2 measurements because in this case the impact of the frontal passage in the ^{222}Rn transport is less sharp. The ^{222}Rn, which is naturally emitted, is widely used as an inert tracer of air masses on different scales (e.g. Arnold *et al.* 2009), and is also useful as an indicator of vertical mixing. It is constantly emitted by terrestrial surfaces and, continental air masses therefore contain greater concentrations of ^{222}Rn (Zahorowski *et al.* 2008). Concentrations of this gas are influenced by both local emissions and horizontal advection. In Cabauw, measurements are recorded at 20 and 200 m agl from 2006 on (see Table 1). ^{222}Rn was studied at Cabauw in 2007 by Zahorowski *et al.* (2008), who focused on diurnal, synoptic and seasonal time-scales. Measurements affected by the mainland European fetch, i.e. for winds blowing from between 50° and 220°, give rise to significantly higher ^{222}Rn concentrations. That range coincides approximately with the one we used to define the offshore flow in the SB algorithm (Section 3). Particularly high values are reported for SE flows at 200 m, while ^{222}Rn concentrations in air masses with oceanic footprints take low ^{222}Rn concentrations along. van der Laan *et al.* (2016) inferred the ^{222}Rn surface fluxes from 2007 until 2013 in Cabauw and the surrounding area, and found that the highest values corresponded to the SW wind direction, whereas the lowest were observed from the NE.

Given that mean diurnal cycle amplitudes at 20 m in spring and summer are about 1.3-1.4 Bq m^{-3} (Zahorowski *et al.* 2008), some SBF passages trigger significant changes in ^{222}Rn. In particular, some SBFs from the N-NE (15° - 45°) induce a significant increase only at 20 m (Figure 13e), whereas they lead to decreases at 200 m. Furthermore, one SB event from the N-NW (315° - 345°) induces a large jump ($\sim$ 1 Bq m^{-3}) at both 20 and 200 m agl. There is also a single event from the W-SW marked in this case by a significant fall in ^{222}Rn of more than 1 Bq m^{-3} at 20 m, and of around 0.5 Bq m^{-3} at 200 m. These observations disagree with the estimates of van der Laan *et al.* (2016) for the surface fluxes of ^{222}Rn, and must therefore be explained by other processes than the nearby emissions. First, the increase in the wind speed enhances the dilution of ^{222}Rn and consequently produces a fall of its concentration (Ho and Measday 2005; Vargas *et al.* 2015), but on the other hand, the transition from convective to stably stratified conditions builds up ^{222}Rn at lower levels. Another factor is linked to the origin of the air mass: oceanic backgrounds bring markedly smaller concentrations (Arnold *et al.* 2009). However, as commented above for CO_2, the SB circulation leads to the return of continental air masses, with the result that mesoscale footprints (i.e. $L \sim 100$ km) can become of great significance in explaining the variability of ^{222}Rn.

7. Conclusions

This study addresses SB phenomena and their complex interactions with the transport of scalars and local turbulence. We have developed an objective and systematic algorithm to select the SB events from a comprehensive meteorological database of

10 years in Cabauw (The Netherlands), located about 50 km from the sea. Validated and continuous data at different levels along the 213-m measurement tower as well as surface fluxes were measured, providing a complete snapshot of the lower atmosphere. Clear SB front passages were obtained, which are solely driven by mesoscale factors. The algorithm is extendible to other areas, since the mesoscale density flows that arrive in our study site are purely driven by the SB. Furthermore, the algorithm can be adapted for the selection of other mesoscale flows such as katabatic flows and down-valley winds.

We found two main wind directions on the SB days, driven by different large-scale pressure patterns and associated with the main nearby bodies of water: the North Sea and the IJsselmeer and Markermeer lakes. Most of the SBF arrivals occurred in late afternoon/early evening [1400 - 1900 UTC], suggesting that, as observed by other authors, the weakening of thermally driven convection accelerates the inland propagation of SBFs.

In order to explore how local turbulence interacts with the arrival of SBFs, we classified the SB events into three ABL regimes according to the value of the sensible heat flux in the onset: convective, transition and stable regimes.

In the convective ABL regime, the local surface turbulence is virtually unaltered by the arrival of the SB. A slight enhancement of the shear contribution with respect to buoyancy could be quantified, even though the thermally-driven regime is sustained. It appears that the convection itself weakens the SB disturbances.

Under the transition regime, the arrival of the SBF leads to a sudden jump in wind speed, a clear falling trend in the height of the mixing layer, and an enhancement of u_*. Surface heat and CO_2 fluxes remain unchanged. Besides, the estimated shear and buoyancy terms increase more rapidly at the higher levels. We therefore conclude that the onset of the SB accelerates the afternoon transition, and that subsequently the nocturnal stable conditions arrive earlier.

A distinct type of behaviour was observed in the stable regime. At that stage the sensible-heat flux and the vertical gradient of the potential-temperature are already negative. As in the transition regime, the wind speed and u_* are sharply enhanced. In addition, the arrival of the SBF produces an increase in σ_w, which disrupts the surface-layer equilibrium. On the one hand, the increasing trend of the buoyancy - which is already negative - and shear contributions to the turbulent kinetic energy are decelerated. On the other, on the basis of the observed and calculated wind-speed differences between two vertical levels based on MOST theory, we find that the onset of the SB brings the wind profile out of equilibrium with the surface. By comparison with non-SB days within the stable regime we find that this disruption is due to the appearance of the SB. Furthermore, the evolution of the shear capacity indicates that there is a tendency towards a weakly turbulent state on both SB and non-SB days. However, in the case of the SB days the balance between the wind-shear profile and the downward sensible-heat flux breaks down, until the equilibrium is restored somewhat later.

As expected, the maritime density currents are accompanied by moister and colder air masses, even though the frontal discontinuities are constrained by forcings such as the local convective mixing. The SB flows from the lakes bring with them the sharpest jumps in humidity, while in case of the CO_2, the greatest increases take place for the SB from the North Sea. Since the CO_2-rich air masses are of continental origin, we argue that those increases probably occur due to the return of continental air masses together with the SB circulation, bringing back the excess CO_2 previously advected by offshore flows. In the case of ^{222}Rn, understanding the changes in concentration is more challenging. We find considerable increases and decreases in ^{222}Rn for distinct SB directions both at 20 and 200 m, indicating that not only the footprint of the air masses, but also the recent history and return of continental air masses together explain the observed conditions.

Finally, we can point out that there is a two-way interaction between the SB and local turbulence. On the one hand, daytime convective mixing weakens the SB disturbances and slows down their inland propagation. On the other, depending on the local turbulence conditions the effect of the SB is distinct, occasionally giving rise in turn to sudden increases in turbulence.

Since our observations were spatially limited, subsequent studies in the form of LES numerical simulations should be conducted in order to describe turbulence explicitly and answer questions such as how turbulent convection affects the slowing down of the inland propagation of the SBFs. Furthermore, the ability of the mesoscale models to capture the observed challenging interaction between the SB and turbulence needs to be investigated, in order to obtain a better representation of the afternoon and evening transition by employing more adequate surface-layer parameterisations.

Acknowledgements

This project was funded by the Spanish government project CGL2015-65627-C3-3-R (MINECO/FEDER). Jon A. Arrillaga is supported by the Predoctoral Training Program for Non-Doctorate Researchers of the Department of Education of the Basque government (PRE_2016_2_0160, MOD = B). The first author developed part of the research during a visit to Wageningen University, supported by a EGONLABUR mobility grant from the Basque government (EP_2016_1_0048). We thank the Royal Netherlands Meteorological Institute (KNMI) for the meteorological data from Cabauw. We are also grateful to the Energy Research Centre of The Netherlands (ECN) for the CO_2 and ^{222}Rn data, and we also thank OSI-SAF for the satellite full-resolution Metop data provided.

APPENDIX

Ceilometer

We use the Haar wavelet transform to estimate the MLH from the LD40 ceilometer (Cohn and Angevine 2000). From the convolution of the aerosol backscatter profile $B(z)$ and the Haar wavelet function, integrated between the altitudes z_b and z_t of the profile, and with a the dilation and b the translation of the wavelet, we obtain the wavelet power spectrum coefficients:

$$W_B(a,b) = \frac{1}{a}\int_{z_b}^{z_t} B(z)h(\frac{z-b}{a})dz. \qquad \text{(A1)}$$

Positive values of $W_B(a,b)$ are generally coincident with the top of aerosol layers. However, this method presents problems under certain conditions: e.g. it is reported to have difficulties in both discerning the evening stable boundary layer close to the surface from the remaining residual layer (Di Giuseppe *et al.* 2012), and in the case of the LD40 ceilometer, in detecting the well-mixed CBL. In fact, since some MLH detections can be doubtful, we discarded detections with a quality index below a specific value. For further details about this procedure we refer the reader to de Haij *et al.* (2007).

The LD40 ceilometer at Cabauw was not continuously operational before April 2006 (see Table 1). Data from the CT75 ceilometer are available before that date, but these have a poorer resolution and the wavelet transform has not yet been tested for them. On the other hand, continuous data from the LD40 ceilometer at De Bilt, which is approximately 25 km north-east of Cabauw (see Figure 2), are available for the whole period (2001-2010). In order to check whether MLH estimates from De Bilt the average daily evolution of the MLH for complete overlapping months in Figure A1. Specifically, we chose January and July 2009 since the local forcings in these months are in contrast. Despite some slight differences, such as the higher values of the MLH during night-time in De Bilt especially in July, most probably as a consequence of urban influence, both emplacements are quite well correlated. We therefore used MLH estimates from De Bilt for the whole 10-year period.

Wind profiler

The MLH during convective conditions was estimated from the maximum value in the vertical profile of the structure parameter C_n^2. The backscatter intensity of the electromagnetic signal measured by the wind profiler is proportional to this parameter. Further specifications are given in White *et al.* (1991). The algorithm employed to estimate the MLH from the maximum in the wind-profiler vertical-backscatter profiles, was modified and extended. Instead of only using the vertical beam, a time-averaged backscatter profile from the four oblique beams at profiler vertical sampling resolution was calculated and fitted with a spline function before the maxima were determined. At the most, two maxima from each profile were selected. The most likely MLH was selected automatically on the basis of certain additional criteria, such as time-height continuity and the spectral width of the Doppler spectrum.

The wind profiler is a very powerful tool for detecting the MLH in deep CBLs, but not for the stable ABLs. The most reliable estimates were selected from a manual editing of the first-guess estimates made by the algorithm.

References

Ahmadov R, Gerbig C, Kretschmer R, Koerner S, Neininger B, Dolman AJ, Sarrat C. 2007. Mesoscale covariance of transport and co2 fluxes: Evidence from observations and simulations using the wrf-vprm coupled atmosphere-biosphere model. *J. Geophys. Res.* **112**(D22): D22 107–, doi:10.1029/2007JD008552, URL http://dx.doi.org/10.1029/2007JD008552.

Antonelli M, Rotunno R. 2007. Large-eddy simulation of the onset of the sea breeze. *J. Atmos. Sci.* **64**(12): 4445–4457, doi:10.1175/2007JAS2261.1, URL http://dx.doi.org/10.1175/2007JAS2261.1.

Arnold D, Vargas A, Ortega X. 2009. Analysis of outdoor radon progeny concentration measured at the spanish radioactive aerosol automatic monitoring network. *Appl. Radiat. Isot.* **67**(5): 833 – 838, doi:http://dx.doi.org/10.1016/j.apradiso.2009.01.042, URL http://www.sciencedirect.com/science/article/pii/S0969804309000487. 5th International Conference on Radionuclide Metrology - Low-Level Radioactivity Measurement Techniques ICRM-LLRMT'08.

Arrillaga JA, Yagüe C, Sastre M, Román-Cascón C. 2016. A characterisation of sea-breeze events in the eastern cantabrian coast (spain) from observational data and {WRF} simulations. *Atmos. Res.* **181**: 265 – 280, doi:http://dx.doi.org/10.1016/j.atmosres.2016.06.021, URL http://www.sciencedirect.com/science/article/pii/S0169809516301752.

Atkins NT, Wakimoto RM. 1997. Influence of the synoptic-scale flow on sea breezes observed during cape. *Mon. Weather Rev.* **125**(9): 2112–2130, doi:10.1175/1520-0493(1997)125⟨2112:IOTSSF⟩2.0.CO;2, URL https://doi.org/10.1175/1520-0493(1997)125<2112:IOTSSF>2.0.CO;2.

Atkinson B. 1981. *Meso-scale atmospheric circulations*. Academic Press: London, ISBN 9780120659609, URL https://books.google.es/books?id=gStRAAAAMAAJ.

Beljaars ACM, Bosveld FC. 1997. Cabauw data for the validation of land surface parameterization schemes. *J. Clim.* **10**(6): 1172–1193, doi:10.1175/1520-0442(1997)010⟨1172:CDFTVO⟩2.0.CO;2, URL http://dx.doi.org/10.1175/1520-0442(1997)010<1172:CDFTVO>2.0.CO;2.

Borne K, Chen D, Nunez M. 1998. A method for finding sea breeze days under stable synoptic conditions and its application to the swedish west coast. *Int. J. Climatol.* **18**(8): 901–914, doi:10.1002/(SICI)1097-0088(19980630)18:8⟨901::AID-JOC295⟩3.0.CO;2-F, URL http://dx.doi.org/10.1002/(SICI)1097-0088(19980630)18:8<901::AID-JOC295>3.0.CO;2-F.

Bosveld F. 2017. Dataset-description document of the datasets in the cesar database. Technical report, KNMI.

Calmet I, Mestayer P. 2016. Study of the thermal internal boundary layer during sea-breeze events in the complex coastal area of marseille. *Theor. Appl. Climatol.* **123**(3): 801–826, doi:10.1007/s00704-015-1394-1, URL http://dx.doi.org/10.1007/s00704-015-1394-1.

Casso-Torralba P, Vilà-Guerau de Arellano J, Bosveld F, Soler MR, Vermeulen A, Werner C, Moors E. 2008. Diurnal and vertical variability of the sensible heat and carbon dioxide budgets in the atmospheric surface layer. *J. Geophys. Res. Atmos.* **113**(D12): n/a–n/a, doi:10.1029/2007JD009583, URL http://dx.doi.org/10.1029/2007JD009583. D12119.

Chapin F, Matson P, Mooney H. 2002. *Principles of terrestrial ecosystem ecology*. Principles of Terrestrial Ecosystem Ecology, Springer: New York, ISBN 9780387954431, URL https://books.google.es/books?id=OOH1H779-7EC.

Cohn SA, Angevine WM. 2000. Boundary layer height and entrainment zone thickness measured by lidars and wind-profiling radars. *J. Appl. Meteorol.* **39**(8): 1233–1247, doi:10.1175/1520-0450(2000)039⟨1233:BLHAEZ⟩2.0.CO;2, URL https://doi.org/10.1175/1520-0450(2000)039<1233:BLHAEZ>2.0.CO;2.

Comin AN, Miglietta MM, Rizza U, Acevedo OC, Degrazia GA. 2015. Investigation of sea-breeze convergence in salento peninsula (southeastern italy). *Atmos. Res.* **160**: 68 – 79, doi:https://doi.org/10.1016/j.atmosres.2015.03.010, URL http://www.sciencedirect.com/science/article/pii/S0169809515000927.

Crosman ET, Horel JD. 2010. Sea and lake breezes: A review of numerical studies. *Boundary-Layer Meteorol.* **137**(1): 1–29, doi:10.1007/s10546-010-9517-9, URL https://doi.org/10.1007/s10546-010-9517-9.

Cuxart J, Jiménez MA, Prtenjak MT, Grisogono B. 2014. Study of a sea-breeze case through momentum, temperature, and turbulence budgets. *J. Appl. Meteorol. Clim.* **53**(11): 2589–2609, doi:10.1175/JAMC-D-14-0007.1, URL https://doi.org/10.1175/JAMC-D-14-0007.1.

de Haij M, Wauben W, Klein Baltink H. 2007. *Continuous mixing layer height determination using the ld-40 ceilometer: a feasibility study*. Royal Netherlands Meteorological Institute (KNMI): De Bilt, URL http://edepot.wur.nl/62411.

De Tomasi F, Miglietta MM, Perrone MR. 2011. The growth of the planetary boundary layer at a coastal site: a case study. *Boundary-Layer Meteorology* **139**(3): 521–541, doi:10.1007/s10546-011-9592-6, URL http://dx.doi.org/10.1007/s10546-011-9592-6.

Deardorff JW. 1972. Numerical investigation of neutral and unstable planetary boundary layers. *J. Atmos. Sci.* **29**(1): 91–115, doi:10.1175/1520-0469(1972)029⟨0091:NIONAU⟩2.0.CO;2, URL http://dx.doi.org/10.1175/1520-0469(1972)029<0091:NIONAU>2.0.CO;2.

Di Giuseppe F, Riccio A, Caporaso L, Bonafé G, Gobbi GP, Angelini F. 2012. Automatic detection of atmospheric boundary layer height using ceilometer backscatter data assisted by a boundary layer model. *Q. J. R. Meteorol. Soc.* **138**(664): 649–663, doi:10.1002/qj.964, URL http://dx.doi.org/10.1002/qj.964.

Gangoiti G, Millán MM, Salvador R, Mantilla E. 2001. Long-range transport and re-circulation of pollutants in the western mediterranean during the project regional cycles of air pollution in the west-central mediterranean area. *Atmos. Environ.* **35**(36): 6267 – 6276, doi:http://dx.doi.org/10.1016/S1352-2310(01)00440-X, URL http://www.sciencedirect.com/science/article/pii/S135223100100440X.

Grisogono B, Ström L, Tjernström M. 1998. Small-scale variability in the coastal atmospheric boundary layer. *Boundary-Layer Meteorol.* **88**(1): 23–46, doi:10.1023/A:1000933822432, URL http://dx.doi.org/10.1023/A:1000933822432.

Hewson TD. 1998. Objective fronts. *Meteorol. Appl.* **5**(1): 37–65, doi:10.1017/S1350482798000553, URL http://dx.doi.org/10.1017/S1350482798000553.

Ho EC, Measday DF. 2005. A simple model for describing the concentration of 212pb in the atmosphere. *J. Environ. Radioact.* **78**(3): 289 – 309, doi:http://dx.doi.org/10.1016/j.jenvrad.2004.05.008, URL http://www.sciencedirect.com/science/article/pii/S0265931X04001730.

Holtslag AAM, Bruin HARD. 1988. Applied modeling of the nighttime surface energy balance over land. *J. Appl. Meteorol.* **27**(6): 689–704, doi:10.1175/1520-0450(1988)027⟨0689:AMOTNS⟩2.0.CO;2, URL https://doi.org/10.1175/1520-0450(1988)027<0689:AMOTNS>2.0.CO;2.

Hu XM, Xue M. 2016. Influence of synoptic sea-breeze fronts on the urban heat island intensity in dallas–fort worth, texas. *Mon. Weather Rev.* **144**(4): 1487–1507, doi:10.1175/MWR-D-15-0201.1, URL https://doi.org/10.1175/MWR-D-15-0201.1.

Jiménez PA, de Arellano JVG, Dudhia J, Bosveld FC. 2016. Role of synoptic- and meso-scales on the evolution of the boundary-layer wind profile over a coastal region: the near-coast diurnal acceleration. *Meteorol. Atmos. Phys.* **128**(1): 39–56, doi:10.1007/s00703-015-0400-6, URL http://dx.doi.org/10.1007/s00703-015-0400-6.

Johansson C, Smedman AS, Högström U, Brasseur JG, Khanna S. 2001. Critical test of the validity of monin–obukhov similarity during convective conditions. *J. Atmos. Sci.* **58**(12): 1549–1566, doi:10.1175/1520-0469(2001)058⟨1549:CTOTVO⟩2.0.CO;2, URL http://dx.doi.org/10.1175/1520-0469(2001)058<1549:CTOTVO>2.0.CO;2.

Lampert A, Pätzold F, Jiménez MA, Lobitz L, Martin S, Lohmann G, Canut G, Legain D, Bange J, Martínez-Villagrasa D, Cuxart J. 2016. A study of local turbulence and anisotropy during the afternoon and evening transition with an unmanned aerial system and mesoscale simulation. *Atmos. Chem. Phys.* **16**(12): 8009–8021, doi:10.5194/acp-16-8009-2016, URL http://www.atmos-chem-phys.net/16/8009/2016/.

Lenschow DH, Wyngaard JC, Pennell WT. 1980. Mean-field and second-moment budgets in a baroclinic, convective boundary layer. *J. Atmos. Sci.* **37**(6): 1313–1326, doi:10.1175/1520-0469(1980)037⟨1313:MFASMB⟩2.0.CO;2, URL http://dx.doi.org/10.1175/1520-0469(1980)037<1313:MFASMB>2.0.CO;2.

Lothon M, Lohou F, Pino D, Couvreux F, Pardyjak ER, Reuder J, Vilà-Guerau de Arellano J, Durand P, Hartogensis O, Legain D, Augustin P, Gioli B, Lenschow DH, Faloona I, Yagüe C, Alexander DC, Angevine WM, Bargain E, Barrié J, Bazile E, Bezombes Y, Blay-Carreras E, van de Boer A, Boichard JL, Bourdon A, Butet A, Campistron B, de Coster O, Cuxart J, Dabas A, Darbieu C, Deboudt K, Delbarre H, Derrien S, Flament P, Fourmentin M, Garai A, Gibert F, Graf A, Groebner J, Guichard F, Jiménez MA, Jonassen M, van den Kroonenberg A, Magliulo V, Martin S, Martinez D, Mastrorillo L, Moene AF, Molinos F, Moulin E, Pietersen HP, Piguet B, Pique E, Román-Cascón C, Rufin-Soler C, Saïd F, Sastre-Marugán M, Seity Y, Steeneveld GJ, Toscano P, Traullé O, Tzanos D, Wacker S, Wildmann N, Zaldei A. 2014. The bllast field experiment: Boundary-layer late afternoon and sunset turbulence. *Atmos. Chem. Phys.* **14**(20): 10 931–10 960, doi:10.5194/acp-14-10931-2014, URL http://www.atmos-chem-phys.net/14/10931/2014/.

Miller STK, Keim BD, Talbot RW, Mao H. 2003. Sea breeze: Structure, forecasting, and impacts. *Rev. Geophys.* **41**(3): n/a–n/a, doi:10.1029/2003RG000124, URL http://dx.doi.org/10.1029/2003RG000124. 1011.

Millán Millán M, Artíñano B, Palomino I, Bezares JC, Martín M, Salvador R. 1991. *Meso-meteorological studies in the iberian peninsula and western mediterranean area*. Springer US: Boston, MA, ISBN 978-1-4615-3720-5, pp. 371–379, doi:10.1007/978-1-4615-3720-5_32, URL http://dx.doi.org/10.1007/978-1-4615-3720-5_32.

Moeng CH, Sullivan PP. 1994. A comparison of shear- and buoyancy-driven planetary boundary layer flows. *J. Atmos. Sci.* **51**(7): 999–1022, doi:10.1175/1520-0469(1994)051⟨0999:ACOSAB⟩2.0.CO;2, URL http://dx.doi.org/10.1175/1520-0469(1994)051<0999:ACOSAB>2.0.CO;2.

Mooij W, Domis LDS, Hülsmann S. 2008. The impact of climate warming on water temperature, timing of hatching and young-of-the-year growth of fish in shallow lakes in the netherlands. *J. Sea Res.* **60**(1–2): 32 – 43, doi:http://dx.doi.org/10.1016/j.seares.2008.03.002, URL //www.sciencedirect.com/science/article/pii/S1385110108000166. Dynamics of Fish and FishersA symposium on Sustainable Management of Marine Living Resources. Food for Thought: Dynamics of Fish and Fishers.

Pérez-Landa G, Ciais P, Sanz MJ, Gioli B, Miglietta F, Palau JL, Gangoiti G, Millán MM. 2007. Mesoscale circulations over complex terrain in the valencia coastal region, spain – part 1: Simulation of diurnal circulation regimes. *Atmos. Chem. Phys.* **7**(7): 1835–1849, doi:10.5194/acp-7-1835-2007, URL http://www.atmos-chem-phys.net/7/1835/2007/.

Sastre M, Yagüe C, Román-Cascón C, Maqueda G. 2015. Atmospheric boundary-layer evening transitions: A comparison between two different experimental sites. *Boundary-Layer Meteorol.* **157**(3): 375 – 399, URL http://search.ebscohost.com/login.aspx?direct=true&db=aph&AN=110527517&lang=es&site=eds-live.

Simpson J. 1994. *Sea breeze and local winds*. Cambridge University Press, ISBN 9780521452113, URL https://books.google.es/books?id=6WPodgtunqIC.

Sluijter R, Instituut KNM, Leenaers H, Camarasa M, Atlasproducties N. 2011. *De bosatlas van het klimaat*. De Bosatlas, Noordhoff Uitgevers, ISBN 9789001120894, URL https://books.google.es/books?id=zACIpwAACAAJ.

Soler MR, Udina M, Ferreres E. 2014. Observational and numerical simulation study of a sequence of eight atmospheric density currents in northern spain. *Boundary-Layer Meteorol.* **153**(2): 195–216, doi:10.1007/s10546-014-9942-2, URL http://dx.doi.org/10.1007/s10546-014-9942-2.

Steeneveld GJ, Holtslag AAM, Debruin HAR. 2005. Fluxes and gradients in the convective surface layer and the possible role of boundary-layer depth and entrainment flux. *Boundary-Layer Meteorol.* **116**(2): 237–252, doi:10.1007/s10546-004-2730-7, URL http://dx.doi.org/10.1007/s10546-004-2730-7.

Stull R. 1988. *An introduction to boundary layer meteorology*. Atmospheric and Oceanographic Sciences Library, Springer Netherlands, ISBN 9789027727695, URL https://books.google.es/books?id=eRRz9RNvNOkC.

Sun H, Clark TL, Stull RB, Black TA. 2006. Two-dimensional simulation of airflow and carbon dioxide transport over a forested mountain: Part ii. carbon dioxide budget analysis and advection effects. *Agric. For. Meteorol.* **140**(1–4): 352 – 364, doi:https://doi.org/10.1016/j.agrformet.2006.03.016, URL http://www.sciencedirect.com/science/article/pii/S0168192306002103. The Fluxnet-Canada Research Network: Influence of Climate and Disturbance on Carbon Cycling in Forests and Peatlands.

Super I, van der Gon HD, Visschedijk A, Moerman M, Chen H, van der Molen M, Peters W. 2017. Interpreting continuous in-situ observations of carbon dioxide and carbon monoxide in the urban port area of rotterdam. *Atmos. Pollut. Res.* **8**(1): 174 – 187, doi:http://dx.doi.org/10.1016/j.apr.2016.08.008, URL http://www.sciencedirect.com/science/article/pii/S1309104216300228.

Talbot C, Augustin P, Leroy C, Willart V, Delbarre H, Khomenko G. 2007. Impact of a sea breeze on the boundary-layer dynamics and the atmospheric stratification in a coastal area of the north sea. *Boundary-Layer Meteorol,* **125**(1): 133–154, doi:10.1007/s10546-007-9185-6, URL https://doi.org/10.1007/s10546-007-9185-6.

Tijm ABC, Holtslag AAM, van Delden AJ. 1999. Observations and modeling of the sea breeze with the return current. *Mon. Weather Rev.* **127**(5): 625–640, doi:10.1175/1520-0493(1999)127⟨0625:OAMOTS⟩2.0.CO;2, URL http://dx.doi.org/10.1175/1520-0493(1999)127<0625:OAMOTS>2.0.CO;2.

van der Laan S, Manohar S, Vermeulen A, Bosveld F, Meijer H, Manning A, van der Molen M, van der Laan-Luijkx I. 2016. Inferring ^{222}rn soil fluxes from ambient ^{222}rn activity and eddy covariance measurements of co$_2$. *Atmos. Meas. Tech.* **9**(11): 5523–5533, doi:10.5194/amt-9-5523-2016, URL http://www.atmos-meas-tech.net/9/5523/2016/.

van Hooijdonk IGS, Donda JMM, Clercx HJH, Bosveld FC, van de Wiel BJH. 2015. Shear capacity as prognostic for nocturnal boundary layer regimes. *J. Atmos. Sci.* **72**(4): 1518–1532, doi:10.1175/JAS-D-14-0140.1, URL http://dx.doi.org/10.1175/JAS-D-14-0140.1.

Van Ulden AP, Wieringa J. 1996. Atmospheric boundary layer research at cabauw. *Boundary-Layer Meteorol.* **78**(1): 39–69, doi:10.1007/BF00122486, URL http://dx.doi.org/10.1007/BF00122486.

Vargas A, Arnold D, Adame J, Grossi C, Hernández-Ceballos M, Bolivar J. 2015. Analysis of the vertical radon structure at the spanish “el arenosillo” tower station. *J. Environ. Radioact.* **139**: 1 – 17, doi:http://dx.doi.org/10.1016/j.jenvrad.2014.09.018, URL http://www.sciencedirect.com/science/article/pii/S0265931X14002847.

Verkaik JW, Holtslag AAM. 2007. Wind profiles, momentum fluxes and roughness lengths at cabauw revisited. *Boundary-Layer Meteorol.* **122**(3): 701–719, doi:10.1007/s10546-006-9121-1, URL http://dx.doi.org/10.1007/s10546-006-9121-1.

White AB, Fairall CW, Thomson DW. 1991. Radar observations of humidity variability in and above the marine atmospheric boundary layer. *J. Atmos. Oceanic Technol.* **8**(5): 639–658, doi:10.1175/1520-0426(1991)008⟨0639:ROOHVI⟩2.0.CO;2, URL https://doi.org/10.1175/1520-0426(1991)008<0639:ROOHVI>2.0.CO;2.

Wichink Kruit RJ, Holtslag AAM, Tijm ABC. 2004. Scaling of the sea-breeze strength with observations in the netherlands. *Boundary-Layer Meteorol.* **112**(2): 369–380, doi:10.1023/B:BOUN.0000027904.18874.75, URL http://dx.doi.org/10.1023/B:BOUN.0000027904.18874.75.

Wyngaard J. 2010. *Turbulence in the atmosphere*. Cambridge University Press, ISBN 9781139485524, URL https://books.google.es/books?id=YLeBN1qYn-0C.

Zahorowski W, Williams AG, Vermeulen AT, Chambers SD, Crawford J, Sisoutham O. 2008. Diurnal boundary layer mixing patterns characterised by radon-222 gradient observations at cabauw.

Table 1. Technical specifications of the measured variables and fluxes used in this study. Note that within the whole analysed period some instrumentation changes have been carried out (see footnote of the table).

Variables	Height (m, agl)	Instrument	Period
Air Temperature	1.5, 10, 20, 40, 80, 140, 200	KNMI Pt-500 element	01/2001-04/2010
		EPLUSE Pt-1000 element	04/2010-12/2010
Dew point temperature	1.5, 10, 20, 40, 80, 140, 200	Vaisala HMP243	01/2001-04/2010
		EPLUSE 33 polymer sensor	04/2010-12/2010
Wind direction	10, 20, 40, 80, 140, 200	KNMI wind vane	01/2001-12/2010
Wind speed	10, 20, 40, 80, 140, 200	KNMI cup anemometer	01/2001-12/2010
Turbulent fluxes	3	Kaijo-Denki sonic anemometer	01/2001-09/2006
($\overline{u'w'}, \overline{v'w'}, \overline{w'T'}$,	5	Gill R3 sonic anemometer	09/2006-12/2010
, $\overline{w'CO_2'}, \overline{w'q'}$) *		IFM open-path sensor	01/2001-11/2005
		LiCor 7500 open-path sensor	11/2005-12/2010
Atmospheric pressure	10	Paroscientific 1016B-01	01/2001-12/2010
Rain	surface	KNMI rain gauge	01/2001-12/2010
CO_2 concentration	20, 60, 120, 200	LiCor-7000 non-dispersive infrared analyser	01/2001-12/2010
Radon concentration	20, 200	ANSTO, two-filter technique	11/2005-12/2010
Aerosol backscatter	surface	Vaisala-Impulsphysik LD-40 ceilometer	**
Radar backscatter	surface	Vaisala LAP-3000 wind profiler	01/2001-12/2010

* The averaging period of the turbulent fluxes is 10 minutes.

** LD40 ceilometer has been continuously operational only since April 2006 in Cabauw. The CT75 ceilometer in Cabauw and the LD40 ceilometer in De Bilt have been operational during the whole period (01/2001-12/2010). Further details are specified in the text.

Table 2. SB algorithm. First column indicates the filter number; second column the criteria to be fulfilled in order to pass each of the filters; third column, the physical justification of each of the filters; and the fourth column, the absolute percentage of the days that pass each of the filters. From a total of 1230 days entering Filter 1, 102 days finally passed Filter 5. See Section 3 for explanation of the variables used.

Filter	Criteria	Physical justification	Acceptance percentage (%)
1	$V_{850} < 6\,m\,s^{-1}$	Remove strong large-scale winds	31.1
2	$(\Delta\theta_{e,850}/\Delta t) > -1.5^\circ C/6h$	Discard days with synoptic cold fronts	26.5
3	$pp < 0.1\,mm$	Reject rainy events	21.7
4	$\Delta T_{sea,land} > 2^\circ C$	Require a land-sea temperature difference	17.0
5	$\Delta\alpha_{10'} > 45^\circ$ \& $(\overline{\Delta\alpha_{10'}})_{2h} < 15^\circ$ *or* $\Delta\alpha_{10'} > 22.5^\circ$ \& $(\overline{\Delta\alpha_{10'}})_{2h} < 5^\circ$	Select a well-marked wind veering to an onshore direction	8.3

Table 3. Free-convection scales for the convective ABL regime between two hours before and two hours after the SB onset: w_*/u_*, σ_w/w_* and t_*. We show the range of values for all the days. Besides, representative values of buoyancy- and shear-driven CBLs (indicated with B and S respectively) obtained in other studies are introduced. Depending on the type of CBL, buoyancy or shear driven, the time scale is given as $t_{*b} = Z_i/w_*$ or $t_{*s} = Z_i/u_*$.

CABAUW	w_*/u_*	σ_w/w_*	$t_*(min)$
Before SB onset (2h)	3.2 - 5.2	0.3 - 0.8	t_{*b}: 15 - 28
After SB onset (2h)	2.4 - 4.6	0.3 - 1.3	t_{*b}: 15 - 35
OTHER STUDIES			
Deardorff (1972)	$>$ 2.2 (B)	0.6	t_{*b}: 15
Lenschow *et al.* (1980)	-	0.67 (B)	t_{*b}: 17
Moeng and Sullivan (1994)	3.6 (B)	0.63	t_{*b}: 8
	1.6 (B + S)	-	t_{*b}: 8 - 10
	0 (S)	-	t_{*s}: 17
Calmet and Mestayer (2016)	3.3 (B)	-	-

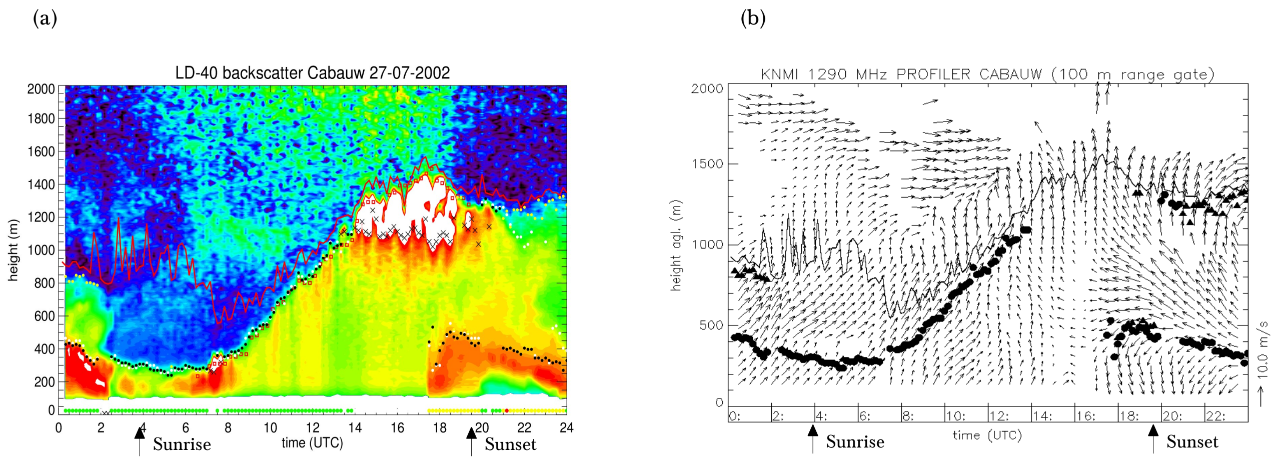

Figure 1. (a) Evolution in time of the aerosol backscatter obtained from the LD40 ceilometer in Cabauw on 27/07/2002. Black circles indicate the mixing-layer height (MLH) estimates. (b) Wind-vector evolution obtained from the wind profiler in Cabauw for the same day. MLH estimates from the LD40 ceilometer are also included with black circles. For further specifications about the figures we refer the reader to de Haij *et al.* (2007), from which the figures were obtained. *Reproduced by kind permission of the authors.*

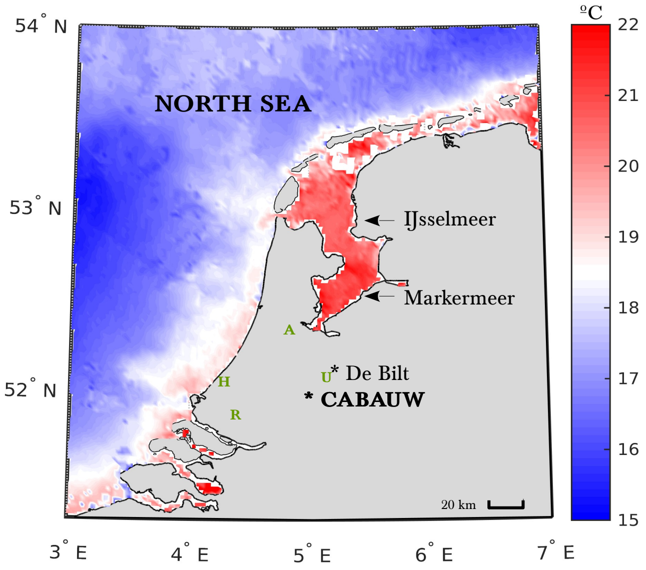

Figure 2. Map showing the area of the coast in the region under study and the mean observed SST for the 28/06/09-02/07/09 period, in which four consecutive SB days were observed. The average SST was computed considering the values at 1000 UTC and 2000 UTC. The SST was obtained from satellite full resolution Metop data (L3P AVHRR, EUMETSAT/OSI SAF 2015). The location of the Cabauw and De Bilt observational sites as well as the seas are shown. Cabauw is around 50 km from both the North Sea and Lake Markermeer. The location of the largest cities within the surrounding area are indicated with initials: A(Amsterdam), U(Utrecht), R(Rotterdam), H(The Hague).

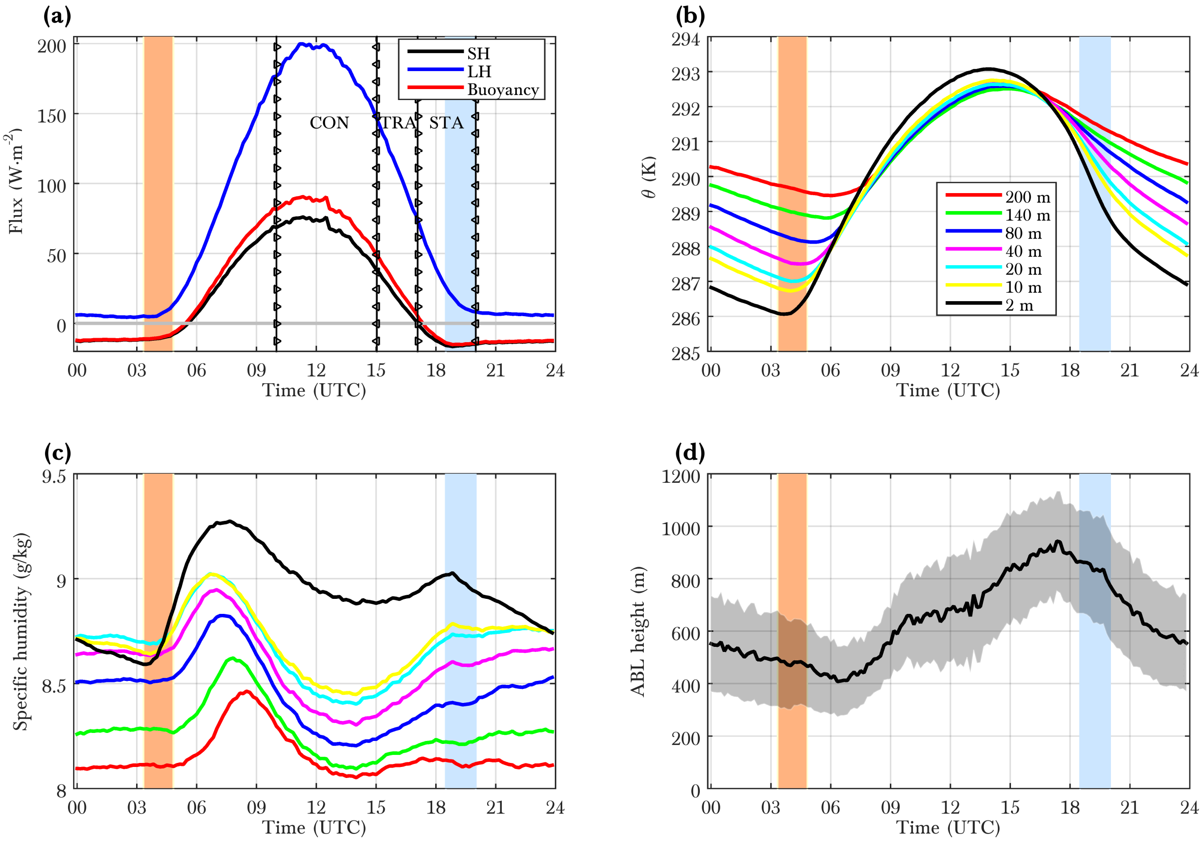

Figure 3. 10-year mean of the diurnal evolution during the warm period (MJJA) of (a) the surface SH, LH and buoyancy fluxes; (b) potential temperature at the different vertical levels; (c) specific humidity at the different vertical levels and (d) estimation of the MLH in De Bilt and its standard deviation (shaded). Only detections with a weak or good quality index are selected for the estimation of the MLH. Shaded vertical bars indicate the sunrise and sunset time ranges for MJJA, in orange and blue respectively. Vertical lines with triangle markers in (a) delimit the SH values for the 3 ABL regimes defined in Section 4 (convective, transition and stable). Local summer time is UTC + 2.

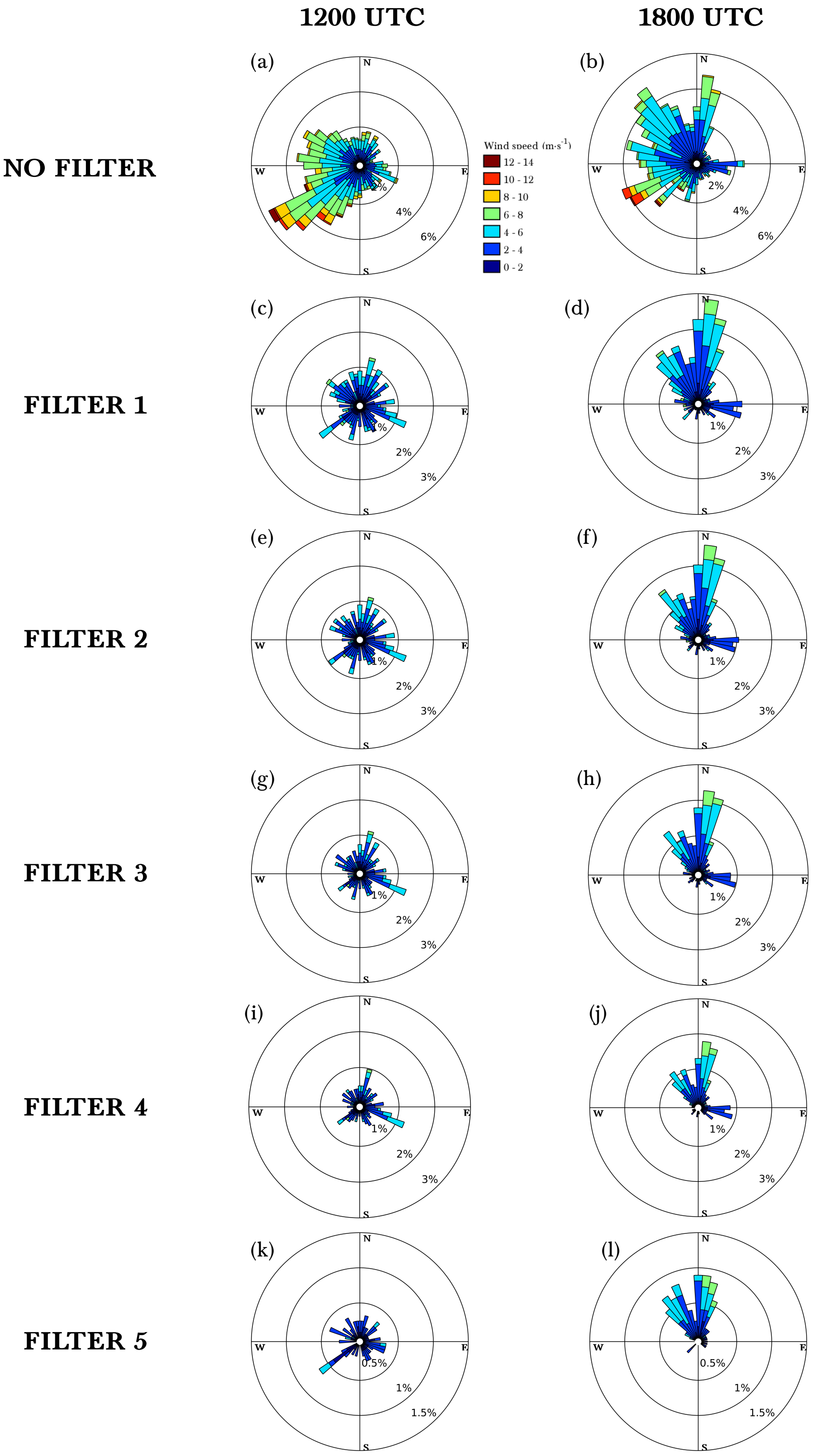

Figure 4. Wind roses for the warm period (MJJA) after application of each filter, on the left at 1200 UTC and on the right at 1800 UTC. Note that the wind-speed scale is the same for all. The scale of the circles represents the percentage of days from all the days that fell within the study period. The 10-m wind measurement is employed in the wind roses.

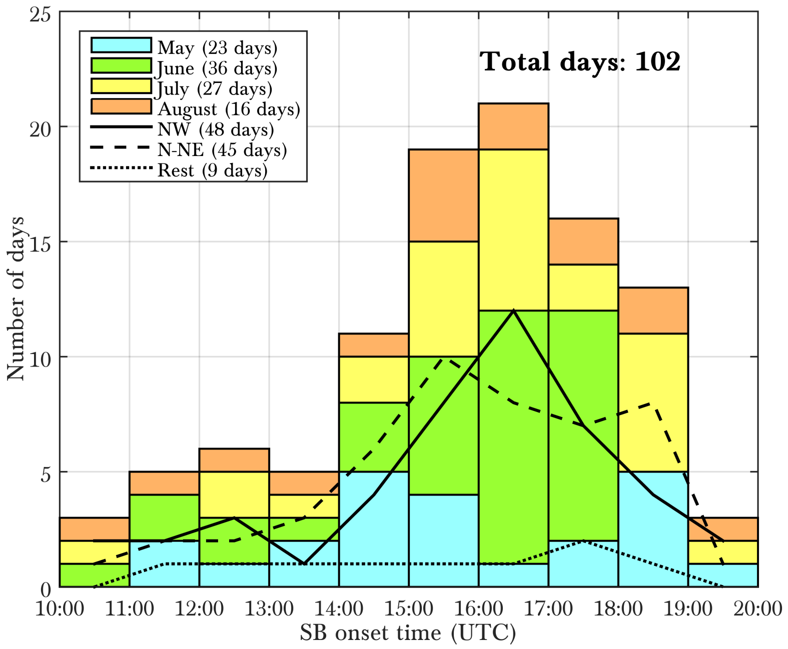

Figure 5. Histogram of times of onset of SB for the individual months (bars) and SB directions just after the onset (lines). The range for defining NW SBs is [290° - 350°] and for N-NE SBs, [350° - 45°]. The other directions are included in the 'Rest' group.

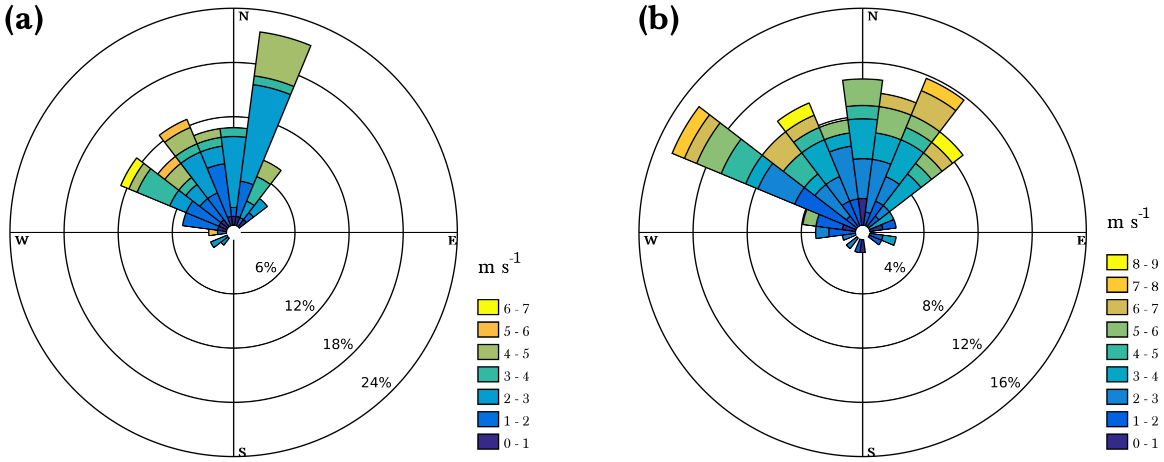

Figure 6. Wind roses of the wind speed at (a) 10 m agl (a) and 200 m agl (b) at the moment of the SB onset. The scale of the circles represents the percentage of days out of the total number of SB days.

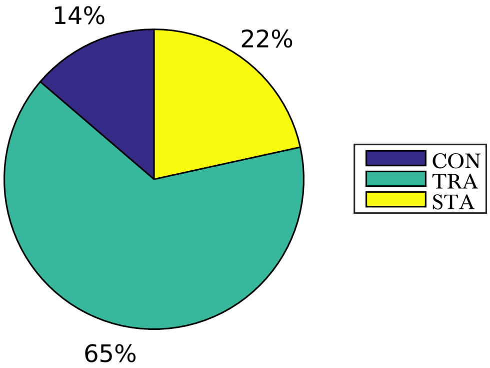

Figure 7. Percentages of the three ABL regimes for the occurrences of SBs: convective regime (CON), transition regime (TRA) and stable regime (STA).

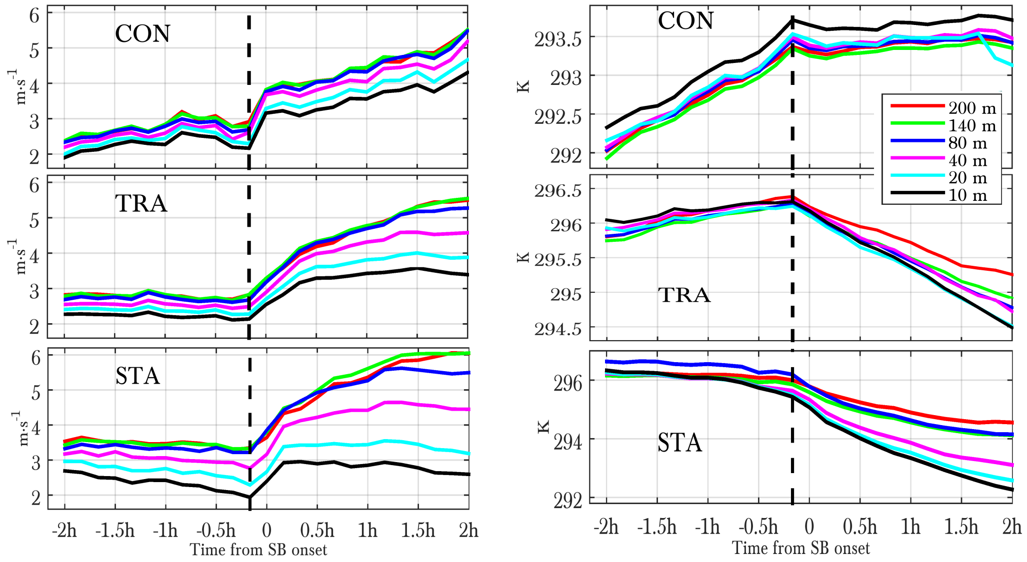

(a) Wind speed

(b) Potential temperature

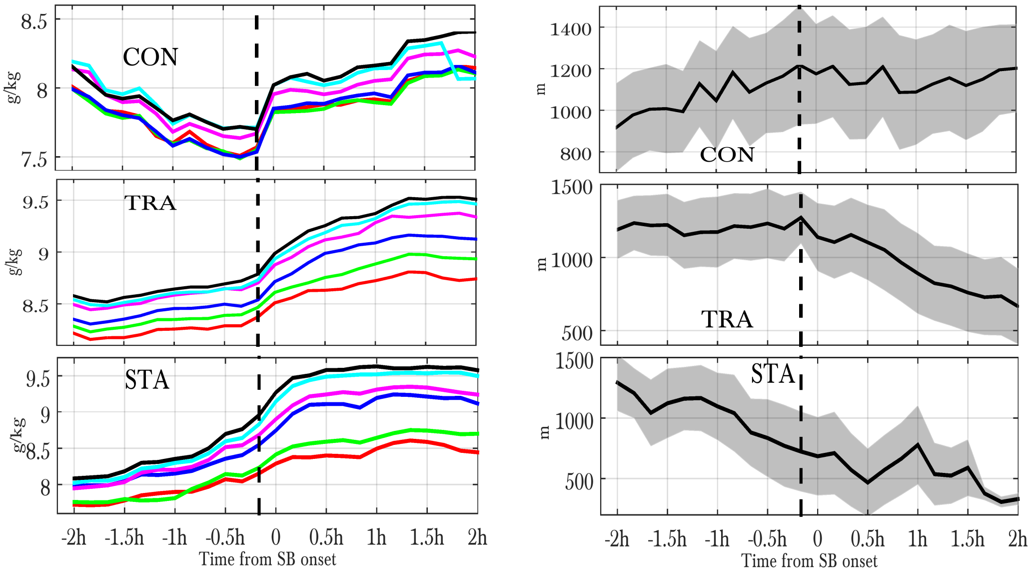

(c) Specific humidity

(d) MLH

Figure 8. Evolution in time of the average (a) wind speed, (b) potential temperature, (c) specific humidity and (d) MLH between two hours before and two hours after the onset of SBs for each of the ABL regimes. The mean for each regime was calculated normalising all the events with respect to the SB onset. The dashed vertical line identifies the 10-minute measurement just before the onset; thus, the onset of SBs occurs between the dashed line and time = 0.

(a) Kinematic buoyancy flux

(b) Surface CO$_2$ flux

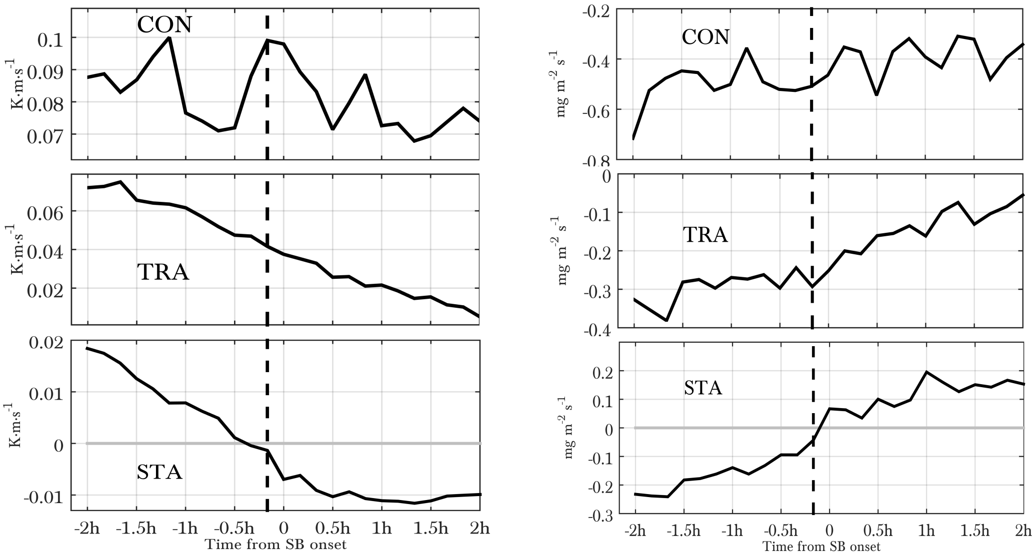

(c) u*

(d) TKE

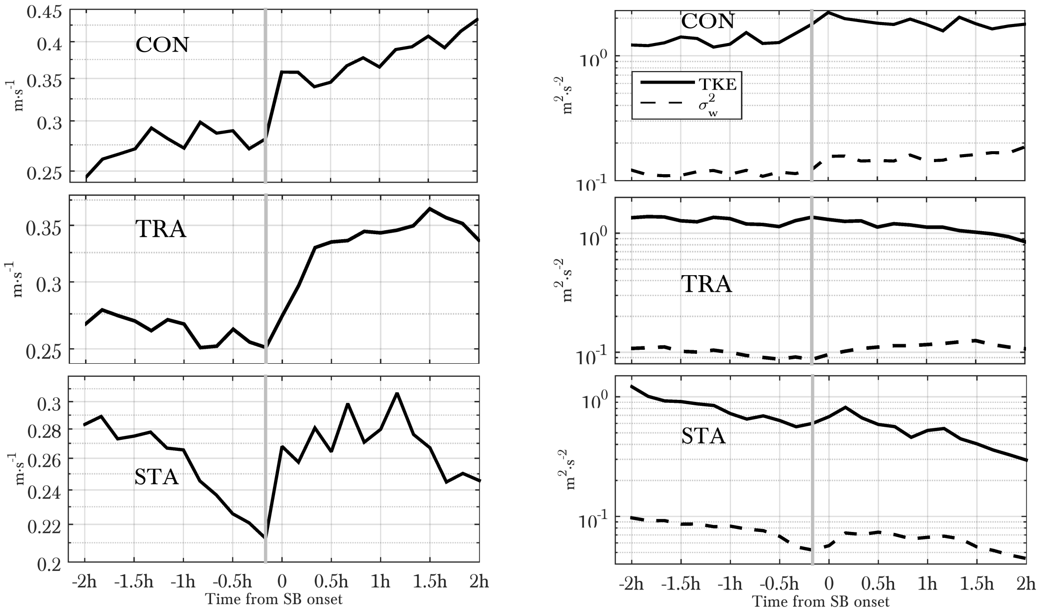

Figure 9. Evolution in time of the average (a) kinematic buoyancy flux, (b) surface CO$_2$ flux, (c) friction velocity and (d) TKE and the variance of the vertical velocity σ_w^2 between two hours before and two hours after the onset of SBs under each of the ABL regimes. The onset is indicated by dashed black vertical lines in (a) and (b), and solid grey vertical lines in (c) and (d).

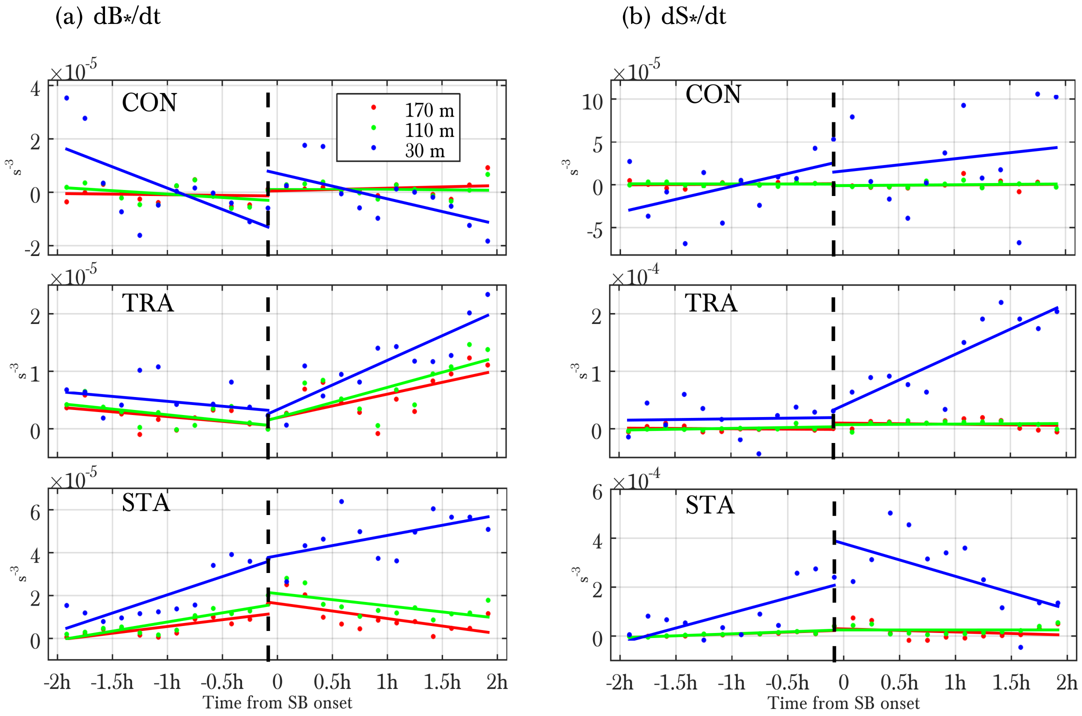

Figure 10. Mean evolution of the temporal derivative of B_* (a) and S_* (b) between two hours before and two hours after the SB onset for each of the ABL regimes at three intermediate vertical levels. The onset of SBs is identified by a dashed vertical line. Dots represent the mean observed values every 10 minutes, while the regression lines are included to depict the trend before and after the onset. Note that 30-minute moving means were calculated in order to smooth the time series.

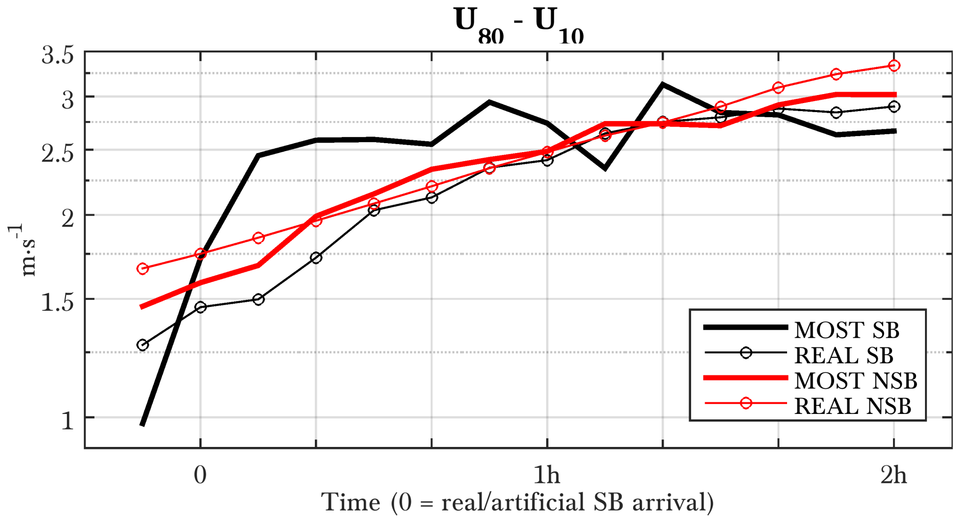

Figure 11. Evolution between the time value before the onset and two hours after it of the average wind-speed difference between 80 and 10 m for the SB days and the NSB days under the stable regime: the solid line represents the wind-speed difference calculated using MOST theory under stable conditions ($\xi = z/L > 0$, see Eq. 13), and the line with circles represents the observed difference (REAL). The events were averaged by being normalised with respect to the SB onset in the case of the SB days and with respect to the artificial SB onset for the NSB days.

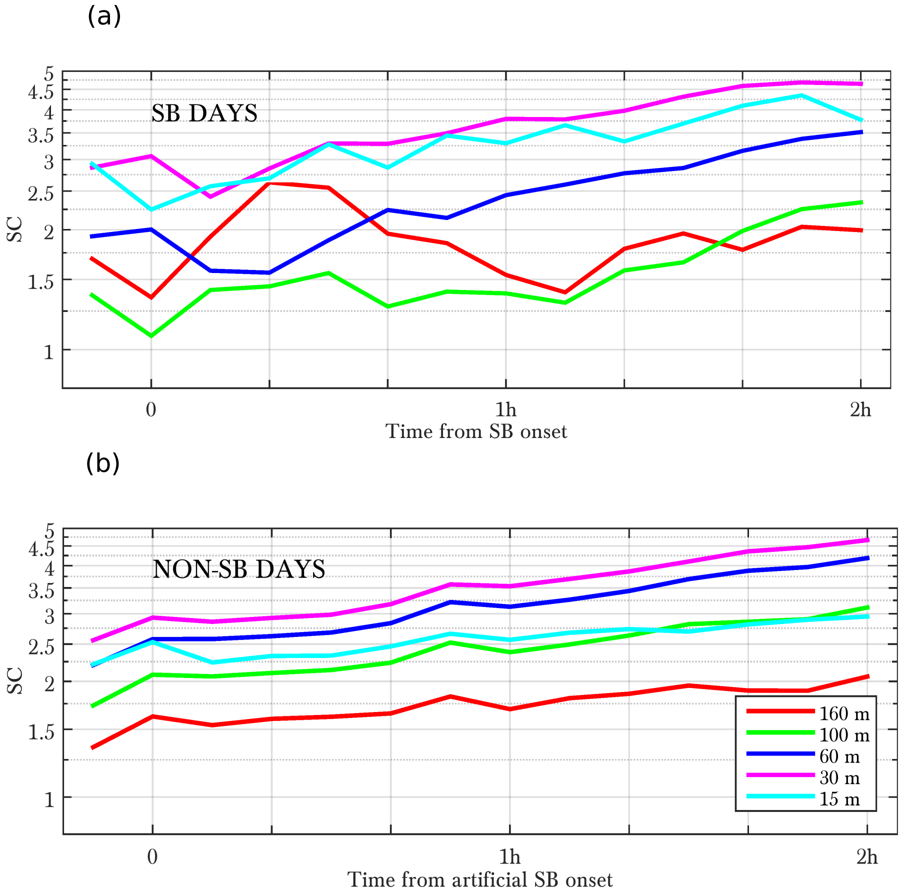

Figure 12. Mean evolution of the SC for SB days (a) and NSB days (b) in the stable ABL regime, between the time value before the real(a)/artificial(b) SB onset and two hours after it. The averages are calculated as in Figure 11.

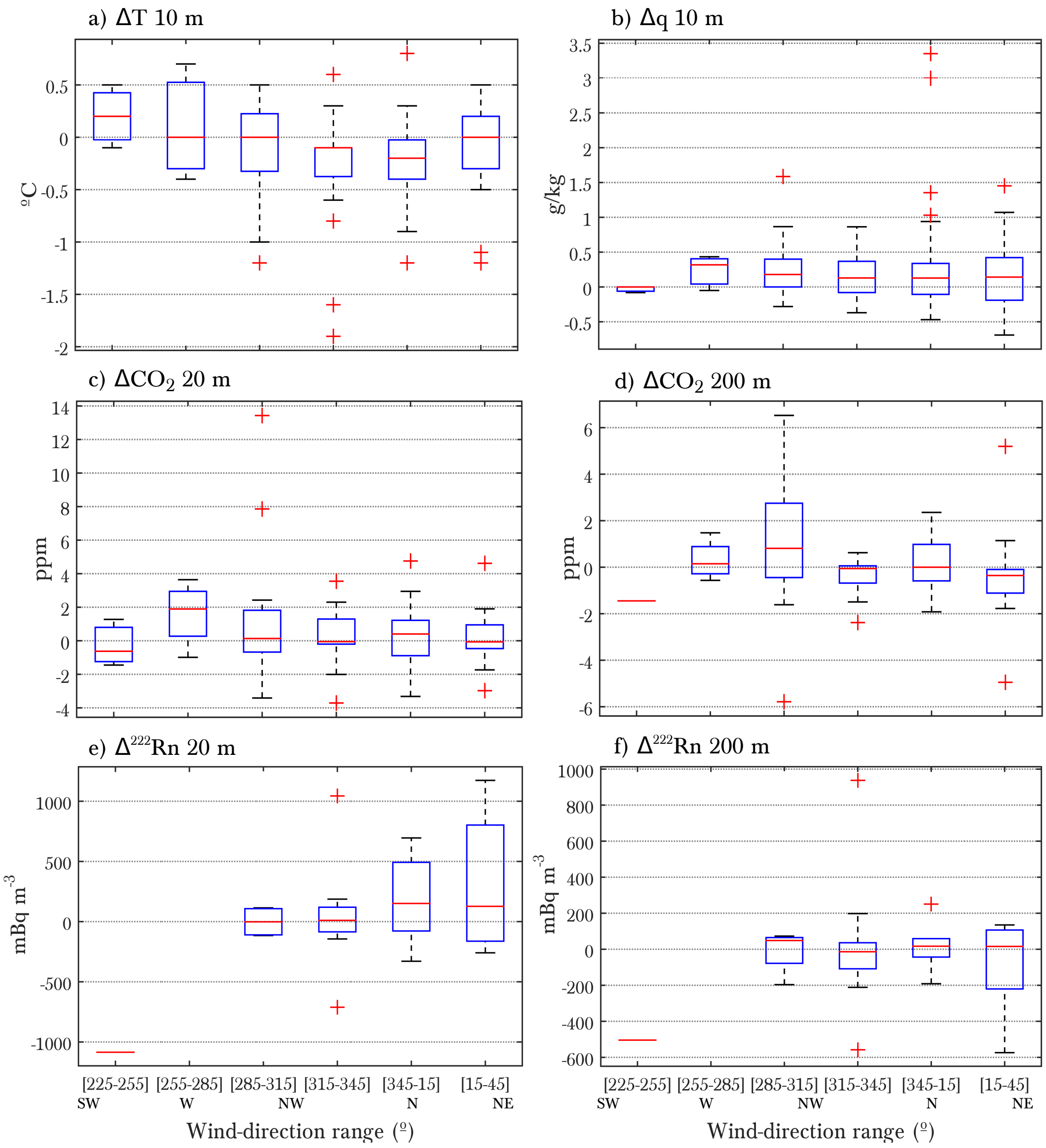

Figure 13. Box plots of the variation in individual variables for different wind-direction ranges: (a) air temperature at 10 m, (b) specific humidity at 10 m, CO_2 at 20 (c) and 200 m (d), and ^{222}Rn at 20 (e) and 200 m (f). The shift in the value of the variable $\psi(t)$ is calculated during the SB onset in (a, b, c, d): $\Delta\psi = \psi(t_{\text{onset}}) - \psi(t_{\text{onset}} - 1)$, i.e. within 10 min in (a, b) and within 30 min in (c, d). In the case of the ^{222}Rn ((e, f)) the change was computed from before the SB onset until 1 h after: $\Delta\psi = \psi(t_{\text{onset}} + 2) - \psi(t_{\text{onset}} - 1)$, i.e. within 90 min. The red horizontal line of the boxplots represents the median, the blue box delimits the first and third quartiles (q_1 and q_3 respectively), the whiskers delimit the most extreme data points not considered to be outliers, and finally, the outliers (red crosses) are drawn if they are greater than $q_3 + 1.5(q_3 - q_1)$ or less than $q_1 - 1.5(q_3 - q_1)$.

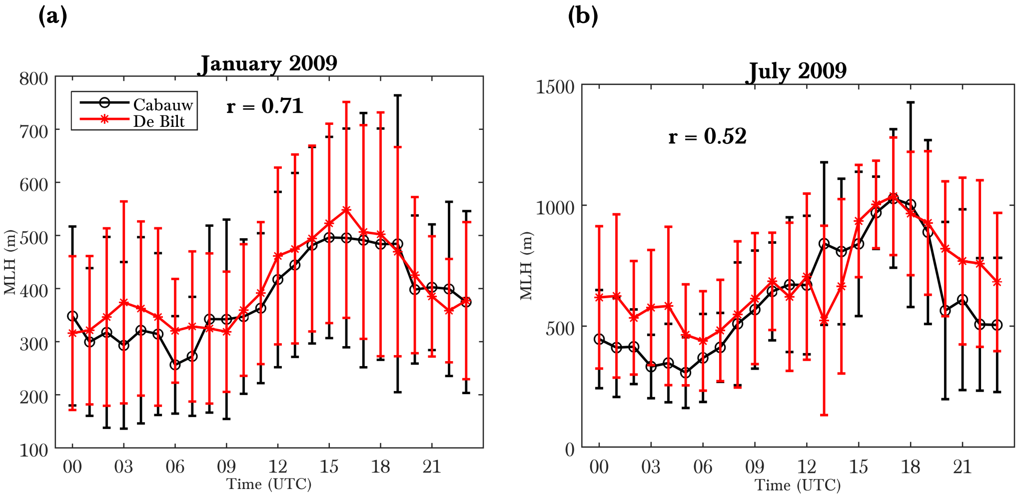

Figure A1. Mean diurnal evolution of the estimated MLH from the LD40 ceilometer at Cabauw and De Bilt for complete overlapping months: (a) January 2009 and (b) July 2009. The error bars indicate the standard deviation of the estimated MLH during each month. The value of the linear-correlation coefficient is also included.